

# How frictional ruptures and earthquakes nucleate and evolve

<https://doi.org/10.1038/s41586-024-08287-y>

Shahar Gvirtzman<sup>1</sup>, David S. Kammer<sup>2</sup>, Mokhtar Adda-Bedia<sup>3</sup> & Jay Fineberg<sup>1</sup>✉

Received: 17 January 2024

Accepted: 24 October 2024

Published online: 8 January 2025

 Check for updates

Frictional motion is mediated by rapidly propagating ruptures that detach the ensemble of contacts forming the frictional interface between contacting bodies<sup>1–7</sup>. These ruptures are similar to shear cracks. When this process takes place in natural faults, these rapid ruptures are essentially earthquakes<sup>8,9</sup>. Although fracture mechanics describe the rapid motion of these singular objects, the nucleation process that creates them is not understood<sup>10–19</sup>. Here we fully describe the nucleation process by extending fracture mechanics to explicitly incorporate finite interface widths (which are generally ignored<sup>20,21</sup>). We show, experimentally and theoretically, that slow steady creep ensues at a well-defined stress threshold. Moreover, as slowly creeping patches approach the interface width, a topological transition takes place in which these creeping patches smoothly transition to the rapid fracture that is described by classical fracture mechanics<sup>22–26</sup>. Apart from its relevance to fracture and material strength, this new picture of rupture nucleation dynamics is directly relevant to earthquake nucleation dynamics; slow, aseismic rupture must always precede rapid seismic rupture (so long as the initial defect in the interface is localized in both spatial dimensions). The theory may provide a new framework for understanding how and when earthquakes nucleate.

Recent experiments<sup>1–7</sup> have validated long-standing predictions<sup>24,27–29</sup> that the onset of frictional motion and earthquake dynamics is governed by rupture fronts that propagate along frictional interfaces. These detach the interlocking contacts forming the interface that provide its resistance to shear. In a natural fault bordered by tectonic plates, this rupture process describes an earthquake<sup>8,9</sup>. The character<sup>5,7,26,30</sup> and dynamics<sup>3,31–34</sup> of these often rapidly propagating ruptures quantitatively correspond to shear cracks described by linear elastic fracture mechanics (LEFM)<sup>22,26</sup>.

Cracks considerably weaken materials, forming singular stresses at their leading edge that focus the elastic energy introduced by external loading. Hence, cracks generally govern material strengths in both bulk materials and frictional interfaces<sup>25,29,35,36</sup>.

Fracture mechanics are relevant only if a crack exists. Otherwise, the resultant stress amplification will not occur, and ruptures will not be excited. Whether a crack nucleates explains why<sup>3,31,37</sup>, under identical nominal conditions, frictional systems are either stable or not<sup>31</sup> over a wide range of imposed initial shear stresses. Rupture nucleation, therefore, determines the onset of frictional motion.

In frictional systems and earthquakes, the preparatory stages of the nucleation process<sup>10–19,38,39</sup> are slow and aseismic. Despite their importance, few detailed experimental descriptions of these processes exist<sup>10,11,18,38,40–43</sup>. Experimentally, frictional nucleation has several puzzling properties that seem to be outside of both LEFM and existing theories of earthquake nucleation<sup>15,44–49</sup>. Recent experiments demonstrated<sup>18,19</sup> that nucleation fronts initiate as two-dimensional (2D) patches that expand at nearly constant velocities,  $v = v_{\text{nuc}}$ , which are two to three orders of magnitude slower than typical rupture velocities.

Moreover, nucleation fronts initiate at scales well below predicted nucleation lengths<sup>15,46,47</sup>, including the Griffith length,  $L_G$ , in LEFM.  $L_G$  and ensuing rupture dynamics are determined<sup>22,31</sup> by energy balance,  $G = \Gamma$ , where  $G$  is the released elastic energy flowing into the tip of a crack and  $\Gamma$ , the fracture energy, is the dissipated energy required to form a unit area of new fracture surfaces. By contrast, nucleation dynamics depend only on the shear stress at the nucleation site beyond a location-dependent threshold stress,  $\tau_{\text{thresh}}$  (refs. 18,19).

LEFM is rigorously formulated for 2D materials, in which cracks are lines with point-like tips. 2D LEFM is valid<sup>25,26,31,50</sup> in three-dimensional (3D) materials, so long as the leading edge of a crack (front) is relatively straight and penetrates the entire width of the material (a through-crack). 2D LEFM also describes 2D penny cracks within infinitely wide interfaces. If we, however, consider 2D rupture patches confined in finite-width interfaces, then LEFM should be modified. This configuration is relevant for earthquakes; the brittle seismogenic zone in which earthquakes often occur has a finite width<sup>20,21,48,49</sup>. By extending LEFM to include these important geometrical effects<sup>51</sup>, we will naturally and quantitatively describe all of the surprising properties characterizing the nucleation phase. This approach, which merges seamlessly with 2D LEFM, introduces new concepts into fracture mechanics such as geometric creep and topological transitions.

## Nucleation as a topological transition

We consider a quasi-2D plate, the dimensions of which in the  $x$  direction (the propagation direction) and  $y$  direction (the normal loading

<sup>1</sup>The Racah Institute of Physics, The Hebrew University of Jerusalem, Jerusalem, Israel. <sup>2</sup>Institute for Building Materials, ETH Zurich, Zurich, Switzerland. <sup>3</sup>CNRS, Laboratoire de Physique ENS de Lyon, UMR5672, Lyon, France. ✉e-mail: jay@mail.huji.ac.il

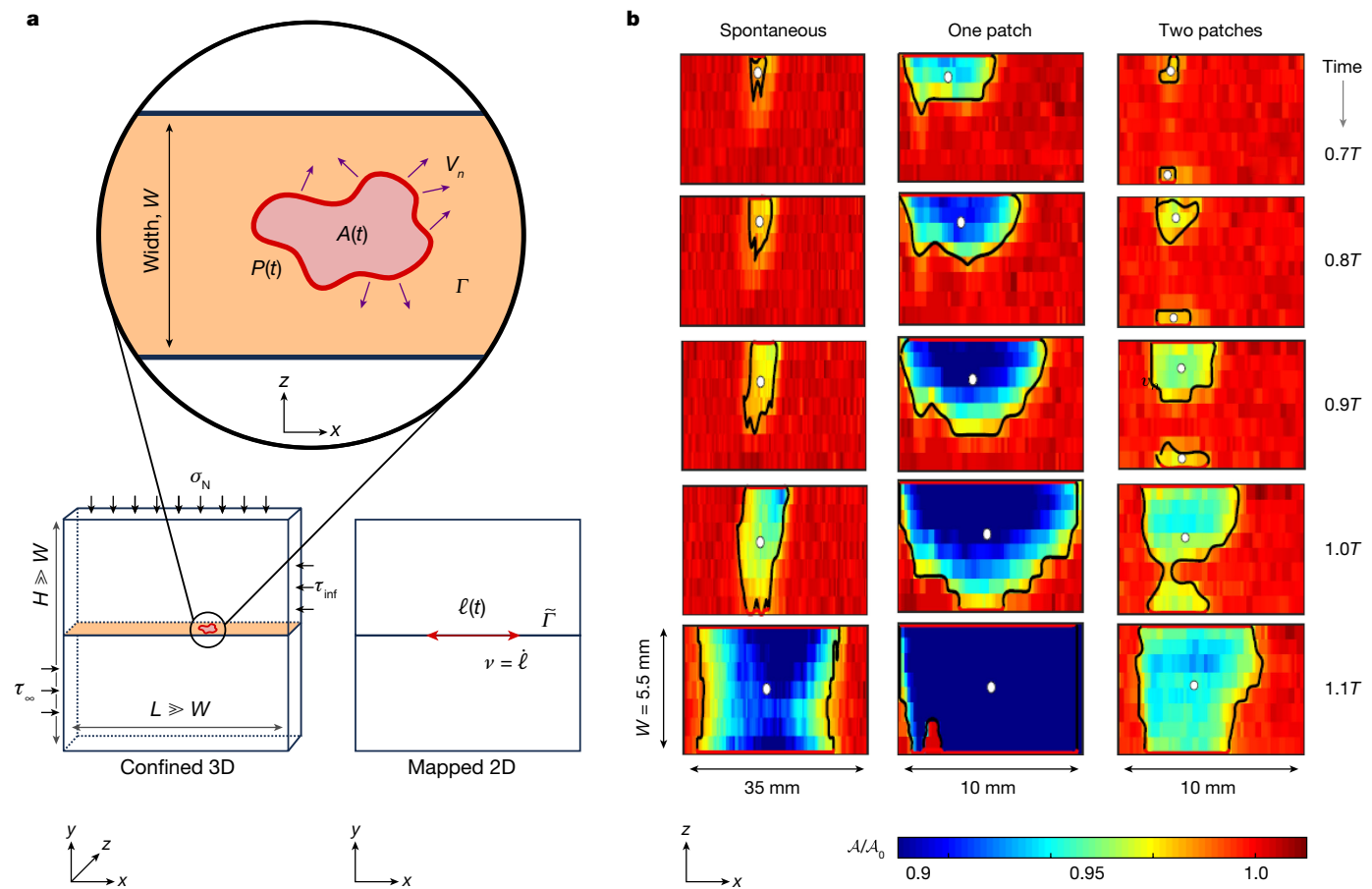


**Fig. 1 | Frictional ruptures nucleate as slowly evolving, confined 2D patches.** **a**, Schematic of frictional failure nucleation in a confined geometry. The system is loaded with a constant normal force,  $\sigma_N$ , and shear force,  $\tau_\infty$ . A crack front with perimeter  $P(t)$  encircles an area  $A(t)$  of broken contacts. The front propagates within an interface of finite width,  $W$ , having a fracture energy,  $\Gamma$ . The interface width,  $W$ , is small compared with the block height,  $H$ , and length,  $L$ . At scales larger than  $W$ , this problem may be mapped to an effective 1D crack of instantaneous length  $\ell(t)$  that is propagating in a 2D material with an effective fracture energy  $\tilde{\ell}$ . **b**, Time evolution of typical

frictional nucleation patches that are visualized by their normalized real contact area,  $\mathcal{A}/\mathcal{A}_0$ . Each nucleating rupture initiates as a 2D patch whose  $P(t)$  is confined within the interface of width  $W = 5.5 \text{ mm}$ . The sequences presented are shown at intervals of  $0.1T$  between times  $0.7T$ – $1.1T$ , where  $T$  is the time between the nucleation onset and the transition to dynamic rupture of the interface. A spontaneous nucleation sequence (left), induced nucleation of a single nucleation patch (centre) and an induced nucleation event in which two nucleation patches simultaneously expanded (right) are shown.

direction) are large relative to its thickness  $W$  along the  $z$  direction (Fig. 1). Plate thicknesses are often ignored or integrated out. Even when considered<sup>20,21,48,49</sup>, crack dynamics are generally assumed to conform to 2D LEFM. This dimension will play an important part by controlling both the dynamics of the nucleation phase and its transition to rapid propagation.

For simplicity, we assume mode II plane-stress loading characterized by uniform shear stress  $\tau_\infty$  imposed at  $y \rightarrow \infty$  and no tractions on plate faces ( $z = 0, W$ ). Consider the stability and motion of a small 2D crack having area  $A(t)$  and perimeter  $P(t)$  (Fig. 1). This confined nucleation patch lies within the  $xz$  plane defining the frictional interface. When  $r$ , the distance from the patch centre, is  $r \gg W$ , the stresses in the plate effectively lose any  $z$ -dependence and the plate becomes approximately 2D under plane-stress conditions. The existence of the patch, however, releases elastic energy relative to a homogeneous plate under the same applied stress (Methods). Hence, from a distance, the patch appears as a through-crack with an effective length,  $\ell$ . 2D LEFM describes the stability and dynamics of this crack by energy balance:  $\tilde{G}(\ell, v) = \tilde{G}_s(\ell) \times g(v) = \tilde{\ell}$ , where  $\tilde{\ell}$  and  $\tilde{G}_s$  are the effective 2D fracture energy and 2D static energy release rate (Methods) and  $g(v)$  is a universal function solely dependent on the instantaneous crack velocity,  $v$  (ref. 22). When  $r < W$ , the through-crack approximation cannot hold and the growing patch is a true 2D crack that dissipates a total energy

per unit extension of  $P(t) \times \Gamma$ , where  $\Gamma$  is the true fracture energy of the material.

Let us see how the outer entities  $\ell$  and  $\tilde{\ell}$  are related to the inner ones,  $A(t), P(t)$  and  $\Gamma$ . To address this, we require two separate conditions that couple the elastodynamic material response to the instantaneous local energy balance at the crack front (Methods). The local dynamics must satisfy two global conditions<sup>51</sup>. First, the dissipation at the perimeter,  $\Gamma \times P(t)$ , must balance the total energy flux  $\int_{P(t)} G$  into the front:

$$\int_{P(t)} G(\zeta, t) d\zeta = \Gamma P(t), \quad (1)$$

$G(\zeta, t)$  is the local mechanical energy released per unit crack advance per unit length of the true crack propagating perpendicular to its front. The second constraint balances the rate of applied work to  $A(t)$  with the creation of a new area,  $\dot{A} = dA/dt$  (or dissipation rate,  $\Gamma \times \dot{A}(t)$ ):

$$\int_{P(t)} V_n(\zeta, t) G(\zeta, t) d\zeta = \Gamma \dot{A}(t), \quad (2)$$

where  $V_n$  is the local normal crack front velocity at every location  $\zeta$  along the front.

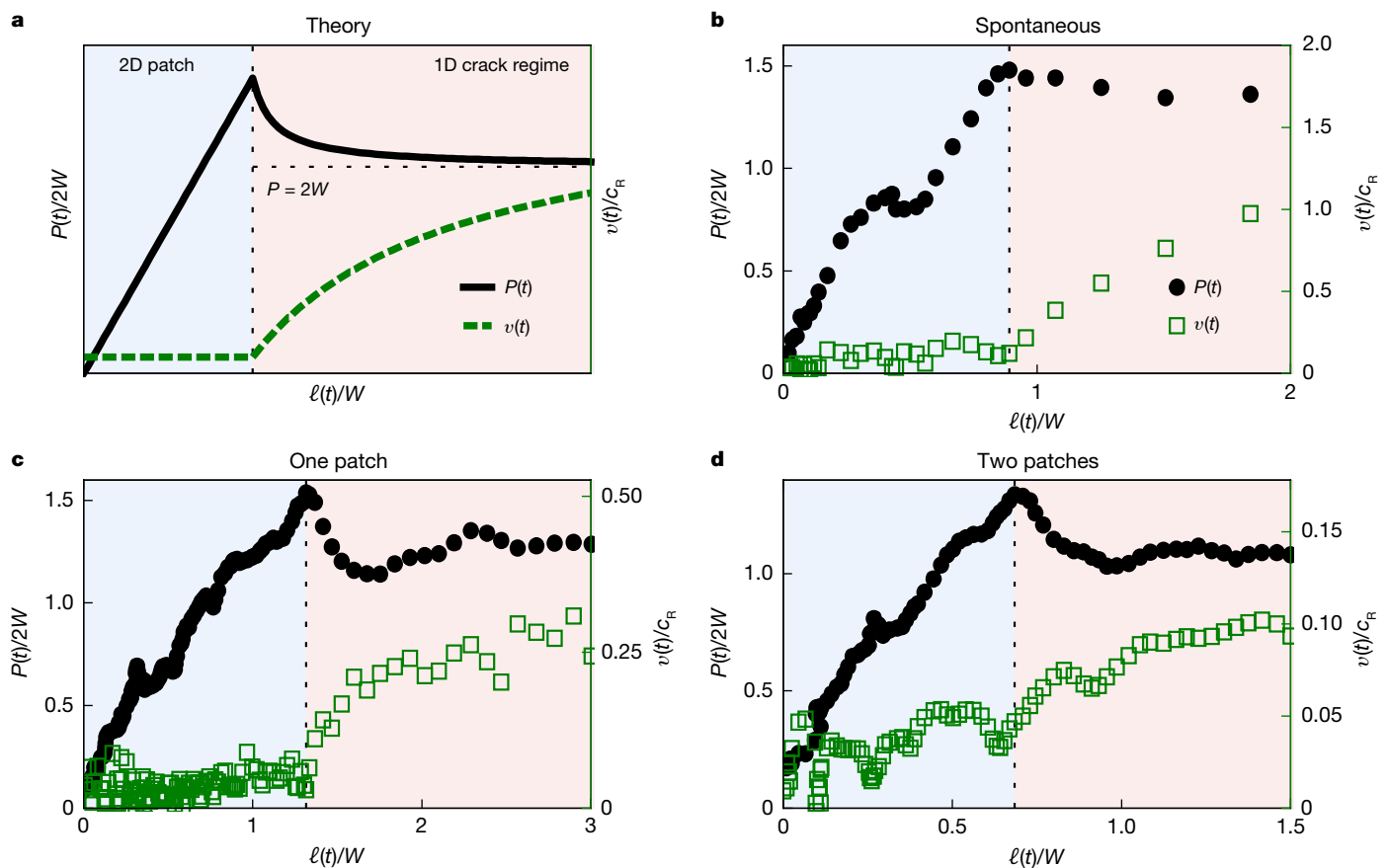


**Fig. 2 | Measured nucleation dynamics undergo the predicted topological transition from confined 2D to rapid 1D rupture fronts.** During the nucleation stage (blue-shaded region), nucleation patches slowly expand at nearly constant velocities, whereas patch perimeters continuously increase. Once the mapped patch size  $\ell$  approaches  $W$ , its perimeter  $P$  reaches its maximal value ( $P(t) \geq 2W$ ) and patch dynamics transition to rapid 2D fracture (red-shaded region).

Equations (1) and (2) must both be satisfied whatever the nucleation patch geometry and/or instantaneous state of the elastic fields in the bulk. In contrast to one-dimensional (1D) cracks, for closed 2D fronts,  $A(t)$  and  $P(t)$  are independent quantities.  $V_n(\zeta, t)$  determines the instantaneous patch geometry and can vary in space and time along  $P$ . Hence, the instantaneous dissipation at  $P(t)$  (equation (1)) and total energy flux into  $A(t)$  (equation (2)) are decoupled. For a bilateral through-crack,  $P = 2W$ , both equations (1) and (2) describe the same energy balance condition, because the crack geometry is fixed;  $V_n(r, \theta) = v_x$  and  $\dot{A}(t) = 2Wv_x$ .

With these conditions, the 2D problem  $(\ell, \tilde{\Gamma})$  is mapped to the 3D problem  $(A(t), P(t), \Gamma)$  by matching the overall dissipation of the inner and outer solutions (Methods):

$$\begin{aligned} \Gamma \times P(t) &= \tilde{\Gamma}(t) \times 2W \\ \Gamma \times \dot{A}(t) &= \tilde{\Gamma}(t) \times \dot{\ell}(t) \times W \end{aligned} \quad (3)$$

$\tilde{\Gamma} = \Gamma P / 2W$  is the effective fracture energy of the mapped through-crack. This mapping defines the effective front velocity,  $v(t) = \dot{\ell}(t) = 2\dot{A}(t)/P(t)$ , as the growth of the area subtended by the patch, with  $\ell(t) = \int^t v(t') dt'$ .

The 2D expression for energy balance now yields

$$\tilde{G}(\ell, v) = \tilde{G}_S(\ell)g(v) = \tilde{\Gamma} = \Gamma \times P(t)/2W \quad (4)$$

For a crack within a plate under a uniform stress drop  $\tau$  (after subtracting the dynamic frictional stress),  $\tilde{G}_S(\ell) = \pi/2 \times \tau^2 \ell/E$  (ref. 22),

a, Qualitative model predictions for  $P(t)$  (black) and  $v(t)$  (green). b–d, Measurements of  $P(t)$  growth and dynamics (black) and  $v(t)$  (green) as a function of the mapped crack size,  $\ell(t) = \int^t v(t') dt'$  where  $v = \dot{\ell} = 2\dot{A}(t)/P(t)$ . Each panel presents  $v(t)$  and  $P(t)$  as a function of  $\ell(t)$ .  $v$  has been scaled by the Rayleigh wave speed,  $c_R$ . Panels b–d correspond to the three examples presented in Fig. 1.

where  $E$  is Young's modulus of the material. Substitution into equation (4) yields

$$g(v) = \frac{2E\Gamma}{\pi W\tau^2} \times \frac{P(t)}{2\ell(t)} \quad (5)$$

Equation (5) results from asymptotic matching of the near-field (3D) to the far-field (2D) solutions. Although not an analytic solution, this procedure encompasses the essential physics of the problem. The far-field solution regulates the energy flux to the crack, which is then used by the near-field crack in accordance with equation (3). This solution qualitatively differs from 3D solutions in the literature (for example, penny-shaped cracks in infinite media); incorporating the finite width,  $W$ , is instrumental in determining the energy flux to the crack.

Important characteristics of equation (5) are as follows:

- Equation (5) fully describes nucleation as a 2D expansion. When the nucleation patch approaches the interface boundaries,  $P \geq 2W$  and  $\ell(t) - W$ , it undergoes a topological phase transition to a real through-crack whose dynamics are described by 2D LEFM. For a straight through-crack,  $P = 2W$  and the LEFM equation of motion,  $g(v) = L_G/\ell$ , is retrieved.  $L_G = 2E\Gamma/(\pi\tau^2)$  is the Griffith (minimal) length for 1D propagation.
- $\beta(t) = \frac{P(t)}{2\ell(t)}$  is a dimensionless factor characterizing the nucleation patch geometry. When the expansion is self-similar,  $\beta$  is constant, and equation (5) yields constant  $v$  for constant  $\tau$  (Methods). These dynamics are unlike the rapid acceleration with  $\ell$  of both 2D LEFM and penny cracks in infinite media.

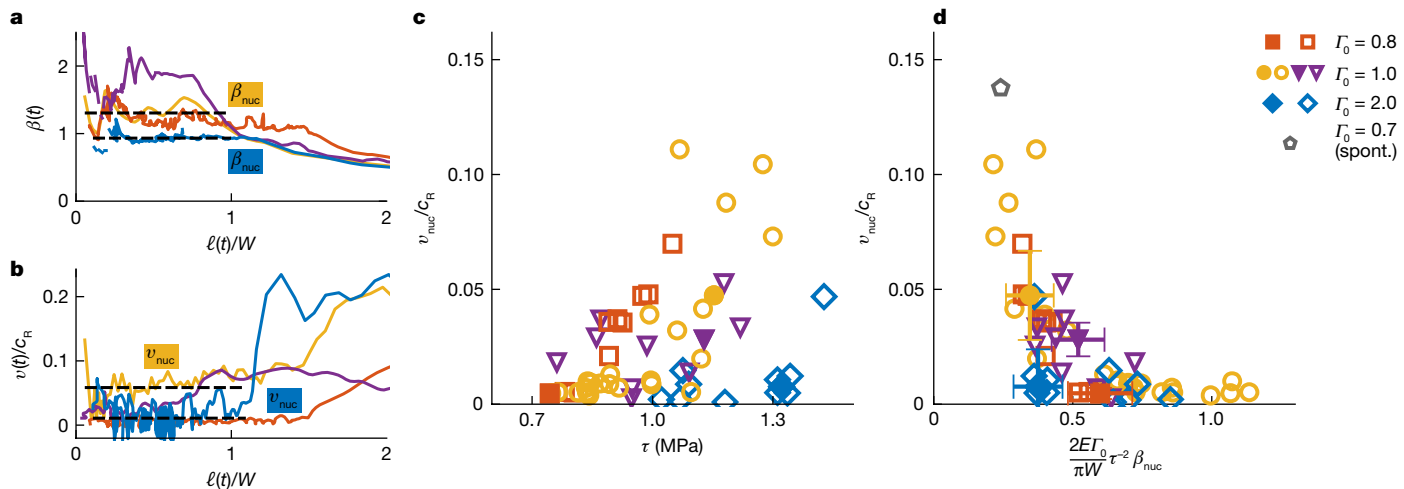


**Fig. 3 | Extending fracture mechanics to confined interfaces quantitatively describes both nucleation patch dynamics and their evolution to fast earthquake-like ruptures.** **a,b,**  $\beta(t) \equiv P(t)/2\ell(t)$  (**a**) and  $v(t)$  (**b**) as a function of  $\ell(t)/W$  for four typical events. Each event has a different nucleation location hence a different geometrical evolution. Dashed horizontal lines indicate the values of  $\beta_{nuc}$  (**a**) and  $v_{nuc}$  (**b**) before the transition to rapid fracture in the yellow and blue events. **c,**  $v_{nuc}$  compared with the shear stress,  $\tau$ , at the point of nucleation of 60 separate experiments. Each symbol colour indicates different experimental

conditions (normal force, nucleation location, geometry of system). Every point corresponds to an entire dynamic sequence (for example, lines in **a** and **b**). The examples in **a** and **b** are denoted by filled symbols. **d,** Collapse of  $v_{nuc}$  data from **c** when plotted against the argument  $(2E\Gamma_0/\pi W)\beta_{nuc}\tau^{-2}$ . The data collapse corresponds to equation (5), with  $v_{nuc}$  the inverse function  $f^{-1}(v_{nuc})$  (with  $f(v) = g(v)/v$ ; see main text). Here,  $\Gamma(v) = \Gamma_0 \times \gamma(v)$ . Typical error bars in  $v$  are noted. The horizontal errors correspond to about twice the point width (Methods).

- $g(v) < 1$  (ref. 22), where  $g(0) = 1$ . Equation (5), therefore, defines a threshold,  $\tau_{thresh} = \sqrt{\frac{2E\Gamma}{\pi W}} \times \beta$ , below which small defects will not expand. In contrast to 2D LEFM, there is no critical (Griffith) length for a nucleating patch. Instead, a stress threshold,  $\tau_{thresh}$ , initiates 2D expansion.  $\tau_{thresh}$  incorporates no critical crack length. Unlike existing nucleation mechanisms,  $\tau > \tau_{thresh}$  initiates rupture patch expansion from size zero.
- Once 2D expansion initiates (assuming constant stress) the patch is guaranteed to reach the boundaries, become a 1D crack, and transition to dynamic rupture (Methods).

These statements are very robust, as they are grounded on general geometrical and topological arguments (Methods).

## Experimental validation

The nucleation process is challenging to accurately measure; a priori when or where nucleation occurs is generally unknown. To overcome this, we developed a method to trigger nucleation at specific locations under controlled and known conditions<sup>18,19</sup> (Methods), by introducing a localized high fracture-energy barrier within the interface. The barrier abruptly arrests propagating ruptures at its near edge, creating a (measurable) stress singularity of the resulting static crack. This enhanced stress induces nucleation of a new rupture front near the opposite (far) edge of the barrier.

In induced nucleation sequences, barriers at different locations triggered diverse nucleation events. Figure 1 includes data from induced nucleation experiments as well as a spontaneous event that nucleated without external triggering. In the same landscape, nucleation events are spatially similar<sup>19</sup>, but evolve at different rates, which are characterized by the time,  $T \approx \alpha/(\tau - \tau_{thresh})$ , between nucleation and dynamic rupture<sup>18</sup>.  $\tau$  and  $\tau_{thresh}$  are the local stress and nucleation thresholds that vary (as does  $\alpha$ ) at each nucleation site.

From the onset of either spontaneous or induced nucleations, we measured the evolution of the real contact area,  $A(t)$  normalized by its value before nucleation,  $A_0$  (Methods and Extended Data Fig. 2). Using  $A(t)/A_0$ , we determine the area  $A(t)$  and perimeter  $P(t)$  of the nucleation patches (Fig. 1b). Far-field mapped quantities,  $v(t)$  and  $\ell(t)$ , are defined by these near-field values (Fig. 1 and equation (3)). Our

experimental observations conform to the predicted qualitative motion and transition dynamics, as nucleation patches evolve from 2D to 1D (Fig. 2). On nucleation,  $P(t)$  increases until  $P \geq 2W$ , as  $\ell(t) \rightarrow W$ . At  $\ell \approx W$ ,  $v$  transitions from slow constant motion to the rapid acceleration of 2D LEFM. This transition occurs when  $P(\ell)$  drops from its peak value to  $P \sim 2W$  characterizing 1D fronts.

The 2D nucleation patch dynamics are characterized by the geometrical factor,  $\beta(\ell) \equiv P(t)/2\ell(t)$ , and  $v(\ell)$ , each function of their mapped (1D) crack lengths  $\ell(t)$ . Both  $v = v(\ell)$  and  $\beta(\ell)$  are fairly constant within the nucleation stage. On their transition to 1D dynamics ( $\ell \approx W$ ),  $v$  accelerates, whereas  $\beta \rightarrow W/\ell$  (Fig. 3a,b). We define the nucleation values of each event,  $\beta_{nuc}$  and  $v_{nuc}$ , as the mean values throughout the 2D regime (Fig. 3a,b). Each  $v_{nuc}, \beta_{nuc}$  point represents an entire dynamic sequence before 2D to 1D transitions.

As in refs. 18,19,  $v_{nuc}$  is a distinct function of  $\tau$  at each location (see Methods for a description of how  $\tau$  is evaluated). The values of  $\ell$  (hence  $\beta_{nuc}$ ) at each transition and the  $\tau$  dependence of  $v_{nuc}$  vary considerably with each nucleation site (Fig. 3). Moreover, the site-dependent nucleation thresholds,  $\tau = \tau_{thresh}$  (refs. 18,19), vary substantially.

We now consider the quantitative predictions of our model. Equation (5) provides an equation of motion for the nucleation process that predicts that  $v$  is a well-defined function of the argument:  $\frac{2E\Gamma}{\pi W\tau^2} \times \beta$ . To test this, we need only the fracture energy,  $\Gamma$ , which was independently measured  $1 < \Gamma < 2 \text{ J m}^{-2}$  (ref. 5) at the mean normal stress of these experiments. Importantly, the argument in equation (5) is the local  $\Gamma$  at the nucleation point. We define  $\Gamma(v) = \Gamma_0 \times \gamma(v)$ , where  $\gamma(v=0) \equiv 1$ . In PMMA,  $\gamma(v)$  varies strongly for the low values of  $v$  that characterize nucleation<sup>52,53</sup>. The argument of equation (5) now becomes  $\frac{2E\Gamma_0}{\pi W\tau^2} \times \beta \times \gamma(v)$ .

Defining  $\xi = \frac{2E\Gamma_0}{\pi W\tau^2} \times \beta$ , equation (5) becomes  $g(v)/v = f(v) = \xi$  (or  $v = f^{-1}(\xi)$ , where  $f^{-1}$  is the inverse function of  $f(v)$ ). Applying  $\xi$  to our data from Fig. 3c yields a good collapse (Fig. 3d). Using  $\Gamma_0$  as a free parameter yields  $0.7 < \Gamma_0 < 2$ , values entirely consistent with measured mean values. Moreover, the functional dependence of all data is, within error bars, identical. Hence, the collapsed data provide values of  $\tau_{thresh}$  at  $\xi \sim 1$ , that quantitatively agree with the theoretical predictions.

Figure 3 shows that the theory correctly predicts the average nucleation speed  $v_{nuc}$  for each experiment. However, the quantitative

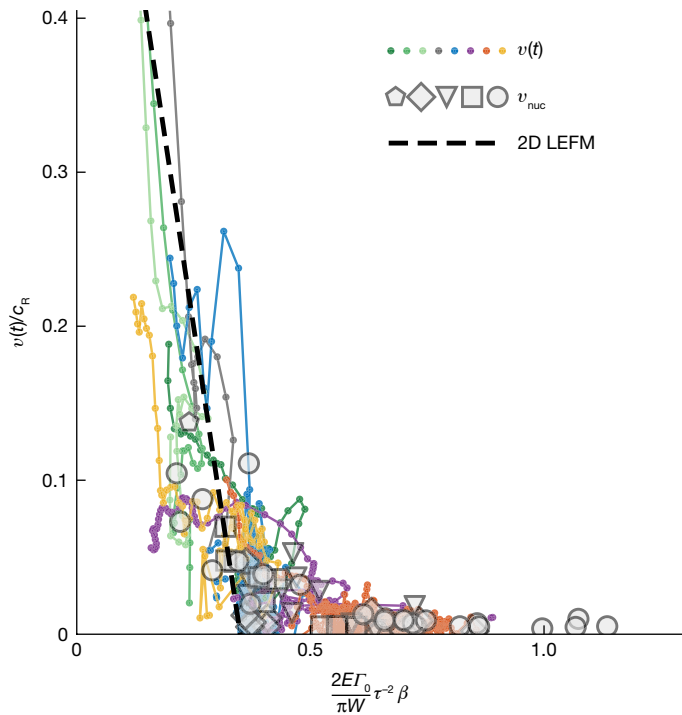


**Fig. 4 | Fracture mechanics seamlessly describe the complete evolution dynamics of nucleation patches as they evolve into rapid ruptures.**

Comparison of the scaling of the quasi-static nucleation velocities,  $v_{\text{nuc}}, \beta_{\text{nuc}}$ , with the corresponding continuous (and instantaneous) dynamics of  $v(t), \beta(t)$ . Symbols correspond to the mean nucleation dynamics ( $v_{\text{nuc}}, \beta_{\text{nuc}}$ ) presented in Fig. 3. Lines are examples of instantaneous rapid dynamics ( $(v(t), \beta(t))$ ) of specific datasets, when scaled as in Fig. 3d in accordance with equation (5). Blue, red, yellow and purple lines correspond to the examples in Fig. 3a,b. Grey lines are data from the spontaneous nucleation event of Fig. 1b. The clear collapse of the dynamic data corresponding to those of Fig. 3 indicates that the nucleation and dynamic processes are the same, once LEFM is extended to include geometrical dynamics. The dashed line indicates 2D LEFM prediction<sup>22</sup> with  $\Gamma = \text{const.}$   $v(t)$  is scaled by the Rayleigh wave speed,  $c_R$ . The errors are as shown in Fig. 3.

predictions of the theory are much broader. In essence, equation (5) represents an energy balance that generalizes 2D LEFM to confined 2D rupture fronts. Equation (5) provides a quantitative description for the entire range of crack dynamics, which also describes 1D front dynamics<sup>22,31,50</sup> when  $\ell(t) \rightarrow W$ . This strong claim is supported by fully dynamic data (Fig. 4, solid lines) that entirely agree with equation (5). Moreover, when  $v$  is a significant fraction of  $c_R, f(v) \rightarrow g(v)$  and rupture dynamics approach the 2D equation of motion<sup>22,31</sup> (dashed line in Fig. 4). This asymptotic prediction agrees well with the data.

## Non-standard rupture in confined geometry

We demonstrated that, in confined systems, the nucleation of frictional ruptures (and earthquakes) is described by extending fracture mechanics to include the confined geometry of an interface (finite thickness,  $W$ ).  $W$  entirely changes both nucleation dynamics and those of rapid frictional ruptures<sup>20,21</sup> and earthquakes<sup>20,21,48,49,54,55</sup>.

So long as nucleation patches are confined, equation (5) predicts a stress threshold value,  $\tau_{\text{thresh}}$ —and not a critical crack length, in contrast to 2D LEFM ( $L_G$ ), friction laws<sup>46</sup> or critical yielding<sup>15</sup>. For  $\tau > \tau_{\text{thresh}}$ , patches initiate at the pixel level (an order of magnitude below  $L_G$  (ref. 18)).

Beyond  $\tau_{\text{thresh}}$  nucleation patches continuously propagate at slow velocities dependent only on  $\tau - \tau_{\text{thresh}}$ . As  $P \rightarrow 2W$ ,  $\tau_{\text{thresh}}$  precisely predicts  $L_G$ . As  $\ell \rightarrow W$ , a sharp (topological) transition to the rapid motion described by 2D LEFM occurs. Equation (5) describes a seamless

transition between these two ostensibly different regimes (Methods). This scenario explains experimental observations of a 2D to 1D transition at the completion of the nucleation process<sup>41,42</sup> in rock, recent field observations<sup>56,57</sup> and numeric observations<sup>48,55</sup> of slow aseismic growth prefacing rapid rupture in confined systems.

It is surprising that as simple an idea as incorporating the patch geometry and system confinement into LEFM yields a wealth of new and unexpected dynamics. The simplicity of the analysis is, perhaps, its greatest strength. The predictions of the theory are entirely general, independent of system complexities. This picture also provides a natural and simple mechanical description of the creep that generally precedes material failure, an important ramification. Creep is commonly observed, but its origins are attributed to a plethora of effects (for example, environmental attack or corrosion of otherwise stable cracks) that are outside of fracture mechanics. Although these effects may have key roles, our picture suggests that they may not always be necessary. The stresses near localized 2D defects simply need to exceed a (well-defined) threshold value.

The picture presented here further provides a clear mechanical and deterministic description of slow (aseismic) preparatory processes that often take place within natural faults before dynamic earthquakes<sup>10</sup>. Our theory predicts that seismically quiet precursory motion will necessarily precede an earthquake, for which the refractory period would depend on both the ambient stress level and fault geometry (for example, the width of the seismogenic layer, or  $W$ ). Although many well-observed earthquakes show no evidence of slow nucleation processes, we surmise that these could occur at small, unresolvable scales.

Our observations are relevant to natural faults because although fault zones are certainly not the thin elastic plates described here, the general physics describing nucleation dynamics should be relevant so long as the elastic energy that drives an earthquake is stored within a brittle elastic seismogenic region whose width is finite compared with the loading dimensions. As a result, the flow of elastic energy driving a nucleation patch is governed by an effective 2D system, whereas the dissipation at the boundaries of the patch is governed by the patch geometry. The specific boundary conditions along the faces of this elastic region should not be expected to qualitatively modify the slow character of the nucleation dynamics. For example, an elastic seismogenic region embedded within slowly creeping plastic regions<sup>21,49</sup> would provide constant stress conditions at the seismogenic boundaries, which, by superposition, are equivalent to the effective plane-stress conditions assumed here. Moreover, slow nucleation patch motion will not induce slip at seismogenic boundaries until the patch approaches them; so even no-slip conditions at seismogenic boundaries should produce similar behaviour.

## Online content

Any methods, additional references, Nature Portfolio reporting summaries, source data, extended data, supplementary information, acknowledgements, peer review information; details of author contributions and competing interests; and statements of data and code availability are available at <https://doi.org/10.1038/s41586-024-08287-y>.

1. Rubinstein, S. M., Cohen, G. & Fineberg, J. Detachment fronts and the onset of dynamic friction. *Nature* **430**, 1005–1009 (2004).
2. Xia, K., Rosakis, A. J. & Kanamori, H. Laboratory earthquakes: the sub-Rayleigh-to-supershear rupture transition. *Science* **303**, 1859–1861 (2004).
3. Passelègue, F. X. et al. Initial effective stress controls the nature of earthquakes. *Nat. Commun.* **11**, 5132 (2020).
4. Schubnel, A., Nielsen, S., Taddeucci, J., Vinciguerra, S. & Rao, S. Photo-acoustic study of subshear and supershear ruptures in the laboratory. *Earth Planet. Sci. Lett.* **308**, 424–432 (2011).
5. Svetlitzky, I. & Fineberg, J. Classical shear cracks drive the onset of dry frictional motion. *Nature* **509**, 205–208 (2014).
6. Wu, B. S. & McLaskey, G. C. Contained laboratory earthquakes ranging from slow to fast. *J. Geophys. Res. Solid Earth* **124**, 10270–10291 (2019).

7. Xu, S., Fukuyama, E. & Yamashita, F. Robust estimation of rupture properties at propagating front of laboratory earthquakes. *J. Geophys. Res. Solid Earth* **124**, 766–787 (2019).
8. Byerlee, J. D. & Brace, W. F. Stick slip, stable sliding, and earthquakes—effect of rock type, pressure, strain rate, and stiffness. *J. Geophys. Res.* **73**, 6031–6037 (1968).
9. Scholz, C. H. *The Mechanics of Earthquakes and Faulting* 3rd edn (Cambridge Univ. Press, 2019).
10. Ohnaka, M. & Shen, L.-F. Scaling of the shear rupture process from nucleation to dynamic propagation: Implications of geometric irregularity of the rupturing surfaces. *J. Geophys. Res. Solid Earth* **104**, 817–844 (1999).
11. Latour, S., Schubnel, A., Nielsen, S., Madariaga, R. & Vinciguerra, S. Characterization of nucleation during laboratory earthquakes. *Geophys. Res. Lett.* **40**, 50564–5069 (2013).
12. Dresen, G., Kwiatek, G., Goebel, T. & Ben-Zion, Y. Seismic and aseismic preparatory processes before large stick-slip failure. *Pure Appl. Geophys.* **177**, 5741–5760 (2020).
13. Popov, V. L., Grzemba, B., Starcevic, J. & Fabry, C. Accelerated creep as a precursor of friction instability and earthquake prediction. *Phys. Mesomech.* **13**, 283–291 (2010).
14. Lapusta, N. & Rice, J. R. Nucleation and early seismic propagation of small and large events in a crustal earthquake model. *J. Geophys. Res. Solid Earth* **108**, 2205 (2003).
15. Uenishi, K. & Rice, J. R. Universal nucleation length for slip-weakening rupture instability under nonuniform fault loading. *J. Geophys. Res. Solid Earth* **108**, 2042 (2003).
16. Hulbert, C. et al. Similarity of fast and slow earthquakes illuminated by machine learning. *Nat. Geosci.* **12**, 69–74 (2019).
17. Leeman, J. R., Marone, C. & Saffer, D. M. Frictional mechanics of slow earthquakes. *J. Geophys. Res. Solid Earth* **123**, 7931–7949 (2018).
18. Gvitzman, S. & Fineberg, J. Nucleation fronts ignite the interface rupture that initiates frictional motion. *Nat. Phys.* **17**, 1037–1042 (2021).
19. Gvitzman, S. & Fineberg, J. The initiation of frictional motion—the nucleation dynamics of frictional ruptures. *J. Geophys. Res. Solid Earth* **128**, e2022JB025483 (2023).
20. Weng, H. & Ampuero, J.-P. The dynamics of elongated earthquake ruptures. *J. Geophys. Res. Solid Earth* **124**, 8584–8610 (2019).
21. Weng, H. & Ampuero, J.-P. Integrated rupture mechanics for slow slip events and earthquakes. *Nat. Commun.* **13**, 7327 (2022).
22. Freund, L. B. *Dynamic Fracture Mechanics* (Cambridge Univ. Press, 1998).
23. Broberg, K. B. *Cracks and Fracture* (Academic Press, 1999).
24. Palmer, A. C. & Rice, J. R. The growth of slip surfaces in the progressive failure of over-consolidated clay. *Proc. R. Soc. Lond. A* **332**, 527–548 (1973).
25. Barras, F. et al. Emergence of cracklike behavior of frictional rupture: The origin of stress drops. *Phys. Rev. X* **9**, 041043 (2019).
26. Barras, F. et al. The emergence of crack-like behavior of frictional rupture: Edge singularity and energy balance. *Earth Planet. Sci. Lett.* **531**, 115978 (2020).
27. Kostrov, B. Selfsimilar problems of propagation of shear cracks. *J. Appl. Math. Mech.* **28**, 1077–1087 (1964).
28. Kanamori, H. & Brodsky, E. E. The physics of earthquakes. *Rep. Prog. Phys.* **67**, 1429–1498 (2004).
29. Viesca, R. C. & Garagash, D. I. Ubiquitous weakening of faults due to thermal pressurization. *Nat. Geosci.* **8**, 875–879 (2015).
30. Mello, M., Bhat, H. S. & Rosakis, A. J. Spatiotemporal properties of Sub-Rayleigh and supershear rupture velocity fields: Theory and experiments. *J. Mech. Phys. Solids* **93**, 153–181 (2016).
31. Svetlizky, I., Kammer, D. S., Bayart, E., Cohen, G. & Fineberg, J. Brittle fracture theory predicts the equation of motion of frictional rupture fronts. *Phys. Rev. Lett.* **118**, 125501 (2017).
32. Kammer, D. S., Svetlizky, I., Cohen, G. & Fineberg, J. The equation of motion for supershear frictional rupture fronts. *Sci. Adv.* **4**, eaat5622 (2018).
33. Bayart, E., Svetlizky, I. & Fineberg, J. Fracture mechanics determine the lengths of interface ruptures that mediate frictional motion. *Nat. Phys.* **12**, 166–170 (2016).
34. Bayart, E., Svetlizky, I. & Fineberg, J. Rupture dynamics of heterogeneous frictional interfaces. *J. Geophys. Res. Solid Earth* **123**, 3828–3848 (2018).
35. Pagliaiungo, F., Passelègue, F., Lebihain, M. & Violay, M. Frictional weakening leads to unconventional singularities during dynamic rupture propagation. *Earth Planet. Sci. Lett.* **626**, 118550 (2024).
36. Brener, E. A. & Bouchbinder, E. Unconventional singularities and energy balance in frictional rupture. *Nat. Commun.* **12**, 2585 (2021).
37. Ben-David, O., Cohen, G. & Fineberg, J. The dynamics of the onset of frictional slip. *Science* **330**, 211–214 (2010).
38. Gori, M., Rubino, V., Rosakis, A. J. & Lapusta, N. Dynamic rupture initiation and propagation in a fluid-injection laboratory setup with diagnostics across multiple temporal scales. *Proc. Natl Acad. Sci. USA* **118**, e2023433118 (2021).
39. Marone, C. in *The Spectrum of Fault Slip Modes from Elastodynamic Rupture to Slow Earthquakes* (eds Bizzarri, A. et al.) *Mechanics of Earthquake Faulting*, Vol. 202, 81–94 (IOS Press, 2019).
40. Guérin-Marthe, S., Nielsen, S., Bird, R., Giani, S. & Di Toro, G. Earthquake nucleation size: evidence of loading rate dependence in laboratory faults. *J. Geophys. Res. Solid Earth* **124**, 689–708 (2019).
41. Fukuyama, E. et al. Spatiotemporal complexity of 2-D rupture nucleation process observed by direct monitoring during large-scale biaxial rock friction experiments. *Tectonophysics* **733**, 182–192 (2018).
42. McLaskey, G. C. Earthquake initiation from laboratory observations and implications for foreshocks. *J. Geophys. Res. Solid Earth* **124**, 12882–12904 (2019).
43. Cebry, S. B. L. & McLaskey, G. C. Seismic swarms produced by rapid fluid injection into a low permeability laboratory fault. *Earth Planet. Sci. Lett.* **557**, 116726 (2021).
44. Dieterich, J. H. Earthquake Nucleation on Faults with Rate-Dependent and State-Dependent Strength. *Tectonophysics* **211**, 115–134 (1992).
45. Ray, S. & Viesca, R. C. Earthquake nucleation on faults with heterogeneous frictional properties, normal stress. *J. Geophys. Res. Solid Earth* **122**, 8214–8240 (2017).
46. Rubin, A. M. & Ampuero, J.-P. Earthquake nucleation on (aging) rate and state faults. *J. Geophys. Res. Solid Earth* **110**, B11312 (2005).
47. Castellano, M., Lorez, F. & Kammer, D. S. Nucleation of frictional slip: a yielding or a fracture process? *J. Mech. Phys. Solids* **173**, 105193 (2023).
48. Chen, T. & Lapusta, N. On behaviour and scaling of small repeating earthquakes in rate and state fault models. *Geophys. J. Int.* **218**, 2001–2018 (2019).
49. Dal Zilio, L., Lapusta, N. & Avouac, J.-P. Unraveling scaling properties of slow-slip events. *Geophys. Res. Lett.* **47**, e2020GL087477 (2020).
50. Goldman, T., Livne, A. & Fineberg, J. Acquisition of inertia by a moving crack. *Phys. Rev. Lett.* **104**, 114301 (2010).
51. Wang, M., Adda-Bedia, M., Kolinski, J. M. & Fineberg, J. How hidden 3d structure within crack fronts reveals energy balance. *J. Mech. Phys. Solids* **161**, 104795 (2022).
52. Vasudevan, A. et al. Adaptation of the tapered double cantilever beam test for the measurement of fracture energy and its variations with crack speed. Preprint at <https://doi.org/10.48550/arXiv.2101.04380> (2021).
53. Scheibert, J., Guerra, C., Célarié, F., Dalmas, D. & Bonamy, D. Brittle-quasibrittle transition in dynamic fracture: an energetic signature. *Phys. Rev. Lett.* **104**, 045501 (2010).
54. Liu, Y. & Rice, J. R. Spontaneous and triggered aseismic deformation transients in a subduction fault model. *J. Geophys. Res. Solid Earth* **112**, B09404 (2007).
55. Galis, M. et al. On the initiation of sustained slip-weakening ruptures by localized stresses. *Geophys. J. Int.* **200**, 890–909 (2014).
56. Liu, C. et al. Complex multi-fault rupture and triggering during the 2023 earthquake doublet in southeastern Türkiye. *Nat. Commun.* **14**, 5564 (2023).
57. Chen, K. et al. Cascading and pulse-like ruptures during the 2019 Ridgecrest earthquakes in the Eastern California shear zone. *Nat. Commun.* **11**, 22 (2020).

**Publisher's note** Springer Nature remains neutral with regard to jurisdictional claims in published maps and institutional affiliations.

Springer Nature or its licensor (e.g. a society or other partner) holds exclusive rights to this article under a publishing agreement with the author(s) or other rightsholder(s); author self-archiving of the accepted manuscript version of this article is solely governed by the terms of such publishing agreement and applicable law.

© The Author(s), under exclusive licence to Springer Nature Limited 2025

## Methods

### Experimental system and analysis

**Sample construction.** Our samples were constructed of poly(methyl-methacrylate) (PMMA) blocks. The  $x, y, z$  dimensions of the top and bottom blocks were, respectively,  $200 \times 100 \times 5.5$  mm and  $290 \times 28 \times 30$  mm. The contact surfaces were optically flat with surface roughnesses (top) of  $3 \mu\text{m}$  and (bottom)  $5 \mu\text{m}$  r.m.s. The longitudinal,  $c_p = 2,680 \text{ m s}^{-1}$ , and transverse  $c_s = 1,361 \text{ m s}^{-1}$ , wave velocities were measured ultrasonically, with a  $\pm 10 \text{ m s}^{-1}$  error. This yields a (plane stress) Rayleigh wave speed of  $c_R = 1,235 \pm 10 \text{ m s}^{-1}$ . PMMA is visco-elastic with a static Young's modulus of  $3.62 \pm 0.3 \text{ GPa}$  and a dynamic Young's modulus of  $E = 5.75 \pm 0.15 \text{ GPa}$ . PMMA has a Poisson ratio of  $\rho = 0.33 \pm 0.0007$  and a density of  $1,170 \pm 10 \text{ kg m}^{-3}$ .

**Loading system.** The loading system used was described, in detail, previously<sup>37</sup>. The top block was clamped at its upper edge and was pressed to the bottom block with a constant external force of  $F_N = 5,000 \text{ N}$  in the  $y$  direction, yielding a mean normal stress of  $4.5 \text{ MPa}$  at the interface. The bottom block was mounted on a low friction translational stage, and stick-slip behaviour occurred spontaneously when the applied shear force,  $F_S$ , was sufficiently high. Once  $F_N$  was set,  $F_S$  was increased continuously at a quasi-static rate ( $50 \text{ N s}^{-1}$ ) in the  $-x$  direction.

**Barrier construction.** As in refs. 18,19, we created a high fracture energy barrier by inscribing a single line of width ranging from  $1 \text{ mm}$  to  $4 \text{ mm}$  across the bottom block in the  $z$  direction, using a blue Staedtler permanent marker of size  $M$ . The presence of the marker increases  $J$  by about a factor of 5 (ref. 18). The effect of the marker could be erased by the use of isopropyl alcohol. By this means, barrier locations were varied in experimental sets.

**Stress measurement at the nucleation points of induced rupture fronts.** Most of the nucleation events described in the main text were induced as in refs. 18,19. Induced nucleation events were excited by spontaneous ruptures, which nucleated near the  $x = 0$  edge and propagated in the  $x$  direction until arresting at the near edge of an imposed barrier. Each arrested rupture formed a singular shear stress,

$$\Delta\sigma_{ij}(v_{\text{arr}}, r, \theta) = K(v_{\text{arr}}) \times \Sigma_{ij}(v=0, \theta) \times (2\pi r)^{-1/2}, \quad (6)$$

where  $\Sigma_{ij}(v, \theta)$  is a known function<sup>22</sup> and  $r, \theta$  are polar coordinates measured from the point of arrest. Equation (6) describes the stress increment due to the singular stress field generated at a rupture front. The full shear stress field is  $\sigma_{xy} = \Delta\sigma_{xy} + \tau_{\text{res}}$ , where  $\tau_{\text{res}}$  is the residual shear stress value that remains after the passage of a rupture<sup>33</sup>. The value of  $\tau_{\text{res}}$  is fairly constant at each point along the interface<sup>33</sup>. We define  $r^*$  as the location (in the vicinity of the far edge of the barrier) of a nucleation event. The value of  $\tau_{\text{res}}(r^*)$  was obtained in our experiments, by interpolation of the measured values of  $\tau_{\text{res}}$  at strain gauges located on either side of  $r^*$ .

$K(v_{\text{arr}})$  in equation (6) is the stress intensity factor created by the initial rupture that was arrested at the near edge of an imposed barrier.  $K(v_{\text{arr}})$  is dependent on the rupture velocity,  $v_{\text{arr}}$ , immediately before the arrest of the rupture. Knowledge of  $K$  provides us with a precise measure of the stress field,  $\tau = \Delta\sigma_{xy}(\delta x)$ , in the vicinity of  $r^*$ , where  $\delta x$  is the distance along the interface between the arrest location and  $r^*$ . As in ref. 19,  $K$  was determined by fitting the strain gauge measurements of the stress changes during rupture propagation and on rupture arrest to equation (6). The strain gauges used for this were located slightly above the interface ( $3.57 \text{ mm} < y_{\text{sg}} < 4.08 \text{ mm}$ ), at locations  $x$  separated by about  $8 \text{ mm}$ . Depending on the location of nucleation events, we used data from strain gauges that were located at  $x_{\text{sg}} = [41.87, 49.36, 57.19, 73.70, 81.53, 89.45, 97.02, 105.36, 113.02, 121.02, 128.43, 135.92, 142.98, 150.72] \text{ mm}$  along the interface. The most precise values of  $K$

were obtained by fitting the component  $\Delta\sigma_{xx}$  of the strain gauge measurements (Extended Data Fig. 1a), as the  $\Delta\sigma_{xx}$  component is both quite large and has no residual stress values. This method for determining  $K$  is different, but equivalent<sup>19</sup>, to the method used previously<sup>18</sup>.

Induced nucleation events are generally generated in stick-slip sequences, in which when we imposed a barrier, each of the rupture events in the sequence generally excited a nucleation event. Some of the arrested ruptures, however, were not sufficiently energetic to trigger nucleation beyond the barrier. When the previously arrested rupture directly excited a nucleation event, the shear stress ahead of the newly arrested rupture is  $\tau = \sigma_{xy} - \tau_{\text{res}}$ . In the cases in which the previously arrested rupture did not trigger a nucleation event, a pre-existing singular field  $\sigma_{xy}^{\text{pre}}$ , at the arrest location was created (Extended Data Fig. 1b). In these cases, as the next rupture did trigger a nucleation event, the values of  $r$  at the nucleation site needed to be corrected to  $\tau = \sigma_{xy}(r^*) - \tau_{\text{res}} + \sigma_{xy}^{\text{pre}}(r^*) = K/\sqrt{2\pi\delta x} + \sigma_{xy}^{\text{pre}}(r^*)$  to account for the pre-existing singularity at the arrest location.

In all events (spontaneous or induced), when  $\sigma_{xy}$  is measured by a strain gauge, the shear stress at the strain gauge,  $\tau_{\text{sg}}$ , is located at  $y_{\text{sg}}$  above the interface. It is possible to<sup>33</sup> improve the estimate of the stress at the interface using  $\tau = \tau_{\text{sg}} + \partial\sigma_{xy}/\partial x \times y_{\text{sg}}$ . When the  $\sigma_{xx}$  gradients are large, this correction may reach as much as 20% of  $\tau$ . These corrections were applied when we used strain gauge data to obtain  $K$ .

The values of  $K$  obtained in this way were in good agreement with the values calculated using

$$\Gamma = G_S \times g(v) = K^2/E \times (1 - \rho^2)g(v), \quad (7)$$

where  $g(v)$  is a universal dynamic function<sup>5,22</sup> that depends on the instantaneous velocity,  $v$ , of the rupture front.  $G_S$  is the static energy release rate.

**Spontaneous nucleation events.** In our experiments we analysed both induced (as described above) and several spontaneous nucleation events that were initiated at locations within the interior of the interface. As we note in Figs. 1–4, both the induced and spontaneous events correspond well to our theoretical predictions. Most of the events analysed here were, however, induced and not spontaneous events. The reasons for using induced events are that induced events enable (1) precise control of the nucleation location, ensuring that nucleation occurs far from technically problematic regions (for example, adjacent to the sample edges) and (2) much more precise regulation of the stress at the nucleation points, which provides us with the capability of slowing down the nucleation to enable precise measurements of both  $v_{\text{nuc}}$  and  $\beta$ .

In general, spontaneous nucleation events were much more difficult to analyse, as they often occurred near the high-stress regions adjacent to the sample corners, at  $x = 0$  or  $x = 200 \text{ mm}$ . Locations near these corners are plagued by large stress gradients. As a result, the stresses at nucleation could not be reliably measured at these points.

Far from these corners, when interior spontaneous nucleation occurred, these events were uncontrolled and often their nucleation dynamics were too rapid to be captured by our imaging techniques. This rendered them unsuitable for detailed analysis. When interior nucleation events were sufficiently slow to enable analysis, they had the distinct advantage that stress measurements were direct. As stress gradients are small within interface interiors, stresses measured at adjacent strain gauges could be used to determine the stresses at nucleation—negating the need to extrapolate the singular stress fields induced by arrested ruptures at the imposed barriers. These spontaneous nucleation events were included in our analysis in the main text. As in the induced events, their dynamics were well-described by equation (5).

**Real contact area measurements.** Changes in the real contact area,  $A(x, z, t)$ , were measured by an optical method based on total internal reflection, as light is transmitted only at contact points<sup>1,5</sup> (for details,

# Article

see ref. 19). The transmitted light intensity is proportional to  $\mathcal{A}(x, z, t)$  and is continuously imaged at a 580,000 frame s<sup>-1</sup> rate. This high frame rate enables us to track the front position within the  $xz$  plane about every 1.7  $\mu$ s. The spatial resolution of the camera of 1,280  $\times$  8 pixels in the  $x \times z$  directions translates to a mapping of 156  $\times$  688  $\mu$ m per pixel in the  $x$  and  $z$  directions, respectively. We illuminate the interface by means of a sheet of incoherent light whose incident angle (about 28°) is far beyond the critical angle for total internal reflection from PMMA to air. As a result, nearly all of the light impinging on non-contacting regions of the interface is reflected away. The transmitted light, which is roughly proportional to  $\mathcal{A}(x, z, t)$ , is imaged by the camera. Rupture patch visualization was accomplished by normalizing each spatial point by its value,  $\mathcal{A}_0(x, z)$ , immediately upon the initial rupture arrest, in cases of induced nucleation, or at a time close to the onset of spontaneous nucleation. This enabled us to detect the small changes in  $\mathcal{A}(x, z, t)/\mathcal{A}_0(x, z)$  that take place during the nucleation phase.

**Determination of  $P(t)$  and  $A(t)$  from the contact area data.** The nucleation patch perimeter,  $P(x, z, t)$ , is defined as the leading edge of each rupture front within the  $xz$  plane. To determine both  $P(x, z, t)$  and the area encompassed within the identified nucleation patch (or patches)  $A(t)$ , we used the following method. We first applied a 0.98 threshold to the normalized contact area measurements, which is slightly above the (0.5–1%) noise level of the camera; every pixel in which  $\mathcal{A}(x, z, t)/\mathcal{A}_0(x, z) < 0.98$  is considered to be broken. We note that the entire decrease in contact area within a nucleation patch is only a few per cent. We checked the threshold range of 0.970–0.985, and no significant influence on the final results was observed. The largest 1 or 2 simply connected patches are first identified. The patch circumferences are then smoothed by a Savitzky–Golay filter, and  $P$  and  $A$  are extracted. The specific smoothing factor for the perimeter was chosen to be such that (small) variations produced no significant influence on the result. This procedure is performed for each frame of the data throughout nucleation patch evolution. To account for any fluctuations of the lighting, the data were then smoothed in time over 4 frames (about 7  $\mu$ s) to produce  $P(t)$  and  $A(t)$ .

The velocities of mapped cracks are defined as  $v \equiv \dot{\ell} = 2\dot{A}(t)/P(t)$ . The mapped length,  $\ell(t)$ , is obtained by temporal integration of  $v$ . The constant,  $I_0$ , of integration was approximated by a linear extrapolation of the  $P(\ell)$  curve to 0; this, in effect, assumes that  $\beta$  is constant at the initial stage of evolution. The values of  $v_{nuc}$  and  $\beta_{nuc}$  were determined by using the mean values of the  $\beta(t)$  and  $v(t)$  over the final part of the nucleation stage. We did not average over the initial phases of  $\beta(t)$  and  $v(t)$  as, in the initial region, the standard deviation of the respective signals is larger than the mean (Fig. 3a,b).

**Error analysis.** Errors in our determination of  $\tau$  were determined as follows.  $\tau$  is defined as the shear stress on the interface at the point of nucleation,  $r^*$ . Once we have determined  $K$ , then  $\tau \equiv K/\sqrt{2\pi r^*} + \sigma_{xy}^{pre}$  (Extended Data Fig. 1). As such,  $\Delta\tau = \tau \times [\Delta K/K + 1/2 \times \Delta r^*/\delta x]$ . We estimate that  $\Delta K \sim 0.005$  MPa m<sup>1/2</sup>, whereas  $K \sim 1$  MPa m<sup>1/2</sup>. Moreover,  $\Delta r^*$  is about 0.3 mm for  $\delta x \sim 2$ –3 mm. This yields an approximate 5–7% measurement error in the values obtained for  $\tau$ .

Errors in  $v_{nuc}$  and  $\beta_{nuc}$  are provided by the standard deviation over the measurement interval used (Fig. 3a,b). Our errors in  $\beta_{nuc}$  typically range from 4–7%, whereas our uncertainty in  $v_{nuc}$  is much larger, typically 30–50%, as the values of  $v_{nuc}$  are generally quite low. Typical error bars for  $v_{nuc}$  are presented in Figs. 3d and 4.

Regarding the argument  $\frac{2E}{\pi W} \times \beta_{nuc} \tau^{-2}$  in Figs. 3d and 4, our typical uncertainty is about  $\pm 10\%$ . This uncertainty is the reason for the considerable scatter in both Figs. 3d and 4.

We estimate our measurement uncertainty in  $\Gamma_0$  to be about  $\pm 0.05$  J m<sup>-2</sup>. This leads to systematic uncertainty of 5% for the largest values of  $\Gamma_0 = 2$  to about 15% for the smallest value,  $\Gamma_0 = 0.7$ . This uncertainty does not contribute to scatter, rather its effect would be to shift

each dataset horizontally in Figs. 3d and 4. This degree of uncertainty does not alter the validity of the results presented, such as the overall collapse of the measurements of  $v$  when scaled by  $\frac{2E}{\pi W} \times \beta_{nuc} \tau^{-2}$ .

## Theoretical derivation of the nucleation of failure in 3D confined geometries

**Overview.** In the theoretical part of this section, for simplicity of presentation, we focus on the nucleation of tensile fracture. Our approach is applicable, however, with no modifications, for the nucleation of frictional failure. In this section, we will first derive the scaling of the elastic fields, released elastic energy and the dissipation functions for three different scaling regimes (for static cracks):

- a penny crack in an infinite 3D system;
  - a through-crack (or tunnel crack) that entirely penetrates the width,  $W$ , of a 3D plate; and
  - the intermediate regime of a penny crack embedded in a 3D plate of finite width  $W$ .
- We will then numerically validate the predicted scaling behaviour for the case of the intermediate regime that is of interest for failure in 3D confined geometries.

Finally, we provide a qualitative dynamic description of confined patch dynamics, a conjecture based on the dimensional reduction of the problem. This description uses recent work<sup>51</sup> that has demonstrated that the 3D nature of real-world materials is especially important in determining the energy dissipation (effective fracture energy) of geometrically complex crack fronts. Based on this, we develop a quasi-2D elastic fracture mechanics framework in which a failure event begins with its growth from a penny-shaped nucleus in a 3D bulk material in a confined (slender) geometry, before transitioning to a through-crack. This mapping approach is relevant for both tensile and shear rupture. We will show that the behaviour of the penny crack in the confined case can be viewed as an effective through-crack in the far field, whereas locally as a regular penny crack. Patch expansion dynamics are calculated by matching the far-field energy release rate to the near-field dissipation (as determined by the geometry of the crack). We will see that the confined case is characterized by a constant expansion rate, as observed in our experiments. This slow and constant expansion rate ( $v_{nuc}$ ) is in sharp contrast to the rapid acceleration (under these loading conditions) of both unconfined penny cracks and real through-cracks.

**Definition of the problem.** Let us first define what we mean by 3D confined geometries. Consider a 3D elastic homogeneous body with a finite thickness  $W$  in the  $z$  direction and infinitely large sizes ( $L_x, L_y$ ) in the  $(x, y)$  directions (Extended Data Fig. 3). At the remote boundaries  $|y| \rightarrow \infty$ , the material is subject to constant and uniform tensile loading. The lateral surfaces  $z = \pm W/2$  of the material are assumed to be traction-free. Consequently, in the absence of defects of any type, the stress field components obey plane-stress conditions, that is  $\sigma_{zx} = \sigma_{zy} = \sigma_{zz} = 0$  is insured at every point in the material. Suppose that a point defect is nucleated at time  $t = 0$  at any given location in the plane  $y = 0$  from which material separation is initiated. At later times  $t > 0$ , a rupture front grows in the  $(x, y = 0, z)$  plane creating a mode I crack patch of area  $A(t)$  and perimeter  $P(t)$ .

At the beginning of the rupture process, the crack surface is bounded by a closed contour in the bulk material. If the growth is sustained, the initial penny shape-like crack front eventually reaches the free boundaries  $z = \pm W/2$  and transitions to a different propagation regime in which two disconnected fronts propagate in opposite directions. This transition, driven by the finite size of the material in the  $z$  direction, is topological in the sense that it consists of a change from a penny-shaped to a through-crack propagation regime. Although the area  $A(t)$  always increases in time, the perimeter  $P(t)$  of the crack front first increases in the penny-shape-like regime, but then decreases and converges to  $2W$  after the transition to the through-crack regime. Using this observation

and energy balance arguments, we will show that this topological phase transition is a prelude to dynamic instability.

Before proceeding further, we will establish some results for an equilibrium penny crack in a confined geometry. These results will allow us to justify the mapping procedure for the dynamics of rupture, shown in Fig. 1 of the main text. This mapping procedure consists of a dimensional reduction of the original 3D problem to an equivalent 2D problem that can be solved analytically.

**2D mapping of the confined 3D geometry.** Consider a 3D elastic body of volume  $\mathcal{V}$  bounded by a 2D contour  $S$  that contains a finite crack of a characteristic area  $A$ . Assume that the material is subjected to a traction distribution  $T_i$  that is applied on  $S$ , whereas the crack surface is traction-free. The elastic response of the material induces displacement  $U_i$  and stress  $\Sigma_{ij}$  distributions. We assume that the material remains at equilibrium: the crack undergoes no propagation under the action of the applied loading. In this case, the total potential energy of the system  $\Omega$  (the sum of the elastic energy and the work exerted by external loading) is given by

$$\Omega = -\frac{1}{2} \int_S T_i U_i dS. \quad (8)$$

The presence of a defect modifies the stress and displacement fields with respect to the homogenous case. Let us define  $\mathbf{U} = \mathbf{u}^{(0)} + \mathbf{u}$  and  $\Sigma_{ij} = \sigma_{ij}^{(0)} + \sigma_{ij}$ , where  $(\mathbf{u}^{(0)}, \sigma_{ij}^{(0)})$  are the elastic fields of the homogeneous medium and  $(\mathbf{u}, \sigma_{ij})$  are the elastic fields induced by a negative traction distribution  $-T_i$  on the crack surface. Therefore, the excess potential energy in the presence of a defect reduces to

$$\Delta\Omega = \Omega - \Omega^{(0)} = -\frac{1}{2} \int_S T_i U_i dS, \quad (9)$$

where  $\Omega^{(0)}$  is the bare total potential energy. The excess potential energy (equation (9)) depends only on the asymptotic behaviour of the displacement field near the remote boundary  $S$ . Thus, it does not involve the asymptotic square root singularity of the stress and strain fields in the vicinity of the crack front. To evaluate  $\Delta\Omega$ , it is enough to compute first-order perturbations of the elastic fields near the remote boundaries induced by the crack surface. If the system is large enough, these perturbations are only given by the dipolar contribution. In the following, we will compute this approximation for different geometries of the system and crack surface. Finally, adding the dissipative energy used to create a crack of area  $A$ , the total energy of the system becomes

$$E_{\text{tot}} = \Delta\Omega + E_{\text{dis}} = -\frac{1}{2} \int_S T_i U_i dS + \Gamma A, \quad (10)$$

where  $\Gamma$  is the so-called fracture energy.

**Scaling behaviour in a 3D geometry (penny crack).** Consider the case of a 3D elastic medium with infinitely large sizes in all of the  $(x, y, z)$  directions. At the remote boundary  $S = 4\pi\rho^2$  with  $\rho = \sqrt{x^2 + y^2 + z^2} \rightarrow \infty$ , the material is subject to constant uniform tensile loading  $T_\rho = \sigma$ . In the presence of a penny-shape-like crack of area  $A \sim R^2$ , the far-field elastic fields that contribute to energy budgeting result from the 3D dipolar field induced by the elastic response of a spherical cavity of size  $R$ . The corresponding stress and displacement fields are simply given by<sup>23</sup>

$$\sigma_{\rho\rho}(\rho) \sim -\frac{\sigma R^3}{\rho^3} \quad \rho \gg R, \quad (11)$$

$$u_\rho(\rho) \sim \frac{\sigma R^3}{\mu \rho^2} \quad \rho \gg R. \quad (12)$$

Therefore, the excess potential energy  $\Delta\Omega_{3D}$  is given by

$$\Delta\Omega_{3D} = -\frac{1}{2} \int_S T_\rho u_\rho dS = -\frac{1}{2} (4\pi\rho^2) \sigma u_\rho \sim -\frac{\sigma^2}{\mu} R^3, \quad (13)$$

and the cost of creating the crack surface is

$$E_{\text{dis}} \sim \Gamma R^2. \quad (14)$$

Note that  $\Delta\Omega_{3D}$  also corresponds to the elastic energy released in the volume  $R^3$  surrounding the crack surface. According to the energy balance criterion of the fracture mechanics framework, crack extension dynamics are determined by the energy release rate,  $G_{\text{penny}} \sim -\frac{1}{R} \partial_R \Delta\Omega_{3D} \sim \frac{\sigma^2}{\mu} R$ .

**Scaling behaviour in an effective 2D geometry (through crack).** We now consider a 3D elastic medium having a finite thickness  $W$  in the  $z$  direction and infinitely large sizes in the  $(x, y)$  directions. At the remote boundaries  $S = 2\pi r W$  with  $r = \sqrt{x^2 + y^2} \rightarrow \infty$ , the material is subject to constant uniform tensile loading  $T_r = \sigma$ . The lateral surfaces  $z = \pm W/2$  of the material are assumed to be traction-free. Consequently, the plane-stress configuration at large scales still holds so long as the crack shape is tunnel-like in the  $z$  direction; a cylindrical cavity of radius  $L/2$  and length  $W$ . For this case, the far-field elastic fields that contribute to energy budgeting result from the resulting 2D dipolar field. The corresponding stress and displacement fields are simply given by

$$\sigma_{rr}(r) \sim -\sigma \frac{L^2}{r^2} \quad r \gg L, \quad (15)$$

$$u_r(r) \sim \frac{\sigma L^2}{\mu r} \quad r \gg L. \quad (16)$$

The excess potential energy is thus given by

$$\Delta\Omega_{2D} = -\frac{1}{2} \int_S T_r u_r dS = -\frac{1}{2} (2\pi r W) \sigma u_r \sim -\frac{\sigma^2}{\mu} L^2 W, \quad (17)$$

and the cost of creating the crack surface is given by

$$E_{\text{dis}} \sim \Gamma L W. \quad (18)$$

Also, in this case,  $\Delta\Omega_{2D}$  is the elastic energy released in the volume  $L^2 W$  surrounding the crack surface, and crack extension is determined by the energy release rate,  $G_{\text{through}} \sim -\frac{1}{W} \partial_L \Delta\Omega_{2D} \sim \frac{\sigma^2}{\mu} L$ .

**Scaling behaviour in a 3D plate having a finite thickness.** Now, consider the same 3D geometry as in the previous section (Extended Data Fig. 3) but assume that a penny-shape-like crack of area  $A \sim R^2$  with  $R < W$  is nucleated in the bulk material at any location in the plane  $y = 0$ . As in the case of a penny crack in infinite medium shown in equation (14), the cost of creating the crack surface depends only on the area of the penny crack,  $E_{\text{dis}} \sim \Gamma R^2$ , and the excess potential energy associated with the crack is of a 3D type (Extended Data Fig. 4a). However, considering the behaviour at the remote boundaries is more complicated, as the crack geometry in the near field breaks the translational symmetry along the  $z$  axis.

Plane-stress conditions, however, still effectively exist at scales  $r = \sqrt{x^2 + y^2} \gg W$ , producing a 2D-type stress field that scales as  $1/r^2$ . Note that the dipolar approximation no longer holds near the crack surface for  $R \ll \rho = \sqrt{x^2 + y^2 + z^2} \ll W$  where the stress field is still of the 3D-type  $\sigma_{rr} \sim 1/\rho^3$ . The stress field in this geometry is therefore given by:

$$\sigma_{rr}(x, y, z) \sim \begin{cases} -\frac{\sigma R^3}{\rho^3} & R \ll \rho = \sqrt{x^2 + y^2 + z^2} \ll W, \\ -\sigma \frac{R}{W} \frac{R^2}{r^2} & r = \sqrt{x^2 + y^2} \gg W. \end{cases} \quad (19)$$

# Article

Equation (19) shows that the stress field is 3D-like at scales  $R \ll \rho \ll W$  and becomes 2D-like when  $r \gg W$ . The continuity of the stress field imposes a matching condition at the crossover  $r \sim W$ . This condition introduces a term  $(R/W)$  in the dipolar approximation of the stress field at  $r \gg W$  that does not appear in the pure 2D geometry (see equation (15)). The asymptotic displacement field near the remote boundaries that contributes to energy budgeting is now given by

$$u_r(r) \sim \frac{\sigma}{\mu} \frac{R^2}{W} r, \quad r = \sqrt{x^2 + y^2} \gg W. \quad (20)$$

The  $1/r$  behaviour of  $u_r(r)$  shows that the relevant dipolar approximation of the elastic fields is now of the 2D plane stress type.

The analytical results of the dipolar approximation are confirmed by numerical simulations (Extended Data Fig. 4b).

The energy release rate is a measure of the local rate of mechanical energy flow out of the material and into the crack front. It is a quantity that is defined per unit crack length. Given the 2D behaviour of the stress field at the remote boundaries, we can obtain an expression for the released elastic energy, by mapping the confined penny crack to an equivalent through-crack with the known 2D behaviour given by equation (17)

$$\Delta\bar{\Omega} \sim -\frac{\sigma^2}{\mu} \ell^2 W, \quad (21)$$

where  $\ell$  is the effective length of the mapped through crack. The energy release rate of this mapped crack will be  $\tilde{G}_{\text{through}} \sim -\frac{1}{W} \partial_\ell \Delta\bar{\Omega} \sim \frac{\sigma^2}{\mu} \ell$ .

As  $G$  should be the same at all scales,  $\tilde{G}_{\text{through}}$  of the mapped through-crack (evaluated at large scales) and  $G_{\text{penny}}$  of the original penny configuration (evaluated near the patch) should be equal. As  $G_{\text{penny}} \sim R$  and  $G_{\text{through}} \sim \ell$ , we therefore find that  $\ell$  must scale with  $R$ . This scaling is also achieved by the mapping described in the main text (equation (3)).

In the case of a confined penny crack, the ratio of the released elastic energy and dissipated energy does not increase with the patch size;  $\Delta\bar{\Omega}/E_{\text{dis}} \sim \ell^2/R^2 = \text{const}$ . This, therefore, predicts no acceleration of the crack with its length, in strong contrast to both the cases of an unconfined penny crack and that of a through-crack, for which  $\Delta\Omega/E_{\text{dis}} \propto R$ .

**Numerical simulations.** To verify the theoretical scaling analysis above, we performed numerical (finite-element) simulations of a static singular crack embedded in a 3D elastic medium  $\mathcal{V}$  with finite thickness  $W \ll H$  and  $W \ll L$ . We solve for static equilibrium and use a small-strain linear elastic constitutive material law with Young's modulus  $E = 1$  GPa and Poisson's ratio  $\rho = 0.25$ . We introduce a penny-shaped crack of radius  $R$  with a sharp front (no process zone) at the centre of the elastic medium and apply a remote tensile load of  $\sigma_\infty = 1$  MPa to the top and bottom boundaries. All other boundaries are traction-free. We make use of all three symmetry planes and model only an eighth of the domain.

We compute the total strain energy in the elastic domain by

$$\Omega_R = \frac{1}{2} \int_{\mathcal{V}} \sum E_{ij} dV, \quad (22)$$

where the subscript  $R$  refers to the radius of the embedded crack. Accordingly,  $\Omega_0$  is the total strain energy in the uncracked domain. We then compute the excess potential energy compared to the uncracked domain with  $\Delta\Omega = \Omega_R - \Omega_0$  and report its dependence on the crack radius in Extended Data Fig. 4a. Our results show a cubic relationship, as expected from the theory described in the previous section.

Furthermore, we measure the stress distribution along a line starting from the centre of the crack and oriented perpendicular to its plane

(that is, along the  $y$  axis). The results show that  $\sigma_{yy}$  follows a  $1/y^3$  relationship near the crack but eventually transitions to a  $1/y^2$  behaviour further away (Extended Data Fig. 4b). The crossover between these two behaviours occurs at  $y \sim W$ , exactly as predicted in equation (19).

**Implications for rupture dynamics.** We have derived the energy and stress field behaviour of cracks that are embedded within a 3D system. Two of these cases, penny cracks in infinite media and through-cracks can be considered as model cases that exhibit full 3D or 2D behaviour, respectively. We then discussed the relevant case for our paper, which is a combination of these two cases—a penny crack embedded within a confined interface. Although the simulations and analytical solutions shown here are for static cracks, it is important to note the ramifications on the dynamics of expanding rupture patches. These dynamics are determined by the energy balance of the fracture energy,  $\Gamma$ , and the energy release rate,  $G$ , at the front of the crack. As shown above, the dissipation energy is a local quantity that is determined in the vicinity of the crack. This results in a 3D-like dissipation per unit crack advance, proportional to  $R$ , that is similar to the case of a penny crack in an infinite medium. By contrast, the stored elastic energy that feeds the crack is a global quantity and is easily calculated at the remote boundaries. This results in 2D-like behaviour, where  $G \sim \ell$ , as in the case of a through-crack.

In the regime in which the crack is still smaller than the confinement width,  $W$ , this combined 3D–2D behaviour will result in a similar scaling with  $\ell \sim R$  of both sides of the energy balance equation that describes the patch propagation. Hence, the expansion of the rupture patch with  $\ell$  in this regime is expected to take place at a constant speed, unlike the known acceleration of a standard crack with  $\ell$  under these loading conditions.

At the topological transition ( $R \rightarrow W$ ), the dissipation loses its  $R$  dependence, whereas  $G$  continues to increase with the crack length  $\ell$ . Hence, at the topological transition, the dynamics of a crack must change markedly; a crack will rapidly accelerate with  $\ell$ , which now becomes the length of a true through-crack (two counterpropagating fronts of length  $W$ ).

Although the results of this section have been established for an equilibrium configuration, we believe (at least when inertial effects are negligible) that they hold when a crack propagates slowly, which is the case of the nucleation process.

In the following, we will implement the general ideas discussed above to the dynamics of an expanding rupture patch.

**Instability at the topological transition.** To guarantee its correspondence with the original 3D problem, the through-crack configuration should satisfy energy budgeting constraints. These conditions must satisfy translational invariance through the thickness at scales far from the crack. This is exactly the case for the instantaneous release rate and the instantaneous energy flow rate. Following ref. 51, we impose the equality of these quantities in both configurations, which yields (see main text)

$$\tilde{\Gamma}(t) = \frac{P(t)}{2W} \Gamma, \quad (23)$$

$$\ell(t) = 2 \int_0^t \frac{\dot{A}(\tau)}{P(\tau)} d\tau. \quad (24)$$

Taking  $A(t) \sim R^2$  and  $P(t) \sim R$ , we retrieve the result for  $\ell(t)$  derived from the dipolar approximation described above.

In light of these results, we can reinterpret the qualitative arguments that follow from Extended Data Fig. 3. Using  $\ell(t)$  instead of  $P(t)$  and  $A(t)$  as the relevant length scale, we show in Extended Data Fig. 5 the generic behaviour of the crack front extension  $P(t)$  of the original problem as a function of the crack length  $\ell(t)$  of the mapped configuration. As  $P(t)$  characterizes (equation (23)) the behaviour of the effective fracture

energy  $\tilde{\Gamma}(t)$ , we see that the mapped problem exhibits non-monotonic dissipative behaviour. In the penny-like failure regime  $\tilde{\Gamma}(t)$  is an increasing function of time (or  $\ell(t)$ ). However, in the through-crack regime,  $\tilde{\Gamma}(t)$  decreases from a peak value to a constant  $\Gamma$  (Fig. 2), creating effective ‘weakening’ behaviour with  $\ell(t)$  that preludes dynamic instabilities. This observation already predicts that the topological transition at  $\ell(t) = \ell^*$  will cause a change in crack propagation dynamics.

Finally, by combining equations (23) and (24), we can write

$$\frac{\tilde{\Gamma}(t)}{\Gamma} = \beta(t) \frac{\ell(t)}{W}, \quad (25)$$

with

$$\beta(t) \equiv \frac{P(t)}{2\ell(t)}. \quad (26)$$

The dimensionless function  $\beta(t)$  is the shape factor of the failure zone. In the through-crack-like failure regime,  $\beta(t)$  converges rapidly to  $W/\ell(t)$ , which corresponds to the case of perfect through-crack propagation. If failure starts within  $|z| < W/2$ , the geometric inequality  $P^2(t) \geq 4\pi A(t)$  always holds during the penny-crack phase, which yields  $\beta(t) \geq \beta_c = \pi/2$ . Although the bound  $\beta_c$  always exists, its magnitude will, however, depend on how and where failure nucleation initiates. In the friction experiments reported in the main text, nucleation could start from the boundaries  $|z| = W/2$  or could involve more than one nucleation patch that allows for a bound  $\beta_c < \pi/2$ .

**Example of energy balance and dynamics of a self-similar penny crack.** The instantaneous dynamic energy release of a moving crack tip in a medium submitted to uniform plane stress traction distribution at its remote boundary is given by<sup>22,23</sup>

$$\tilde{G}(t) = g(v) \frac{K(t)^2}{E}, \quad (27)$$

where  $E$  is the Young modulus,  $v(t) = \dot{\ell}(t)$  and  $K(t)$  is the stress intensity factor given by

$$K(t) = \sigma \sqrt{\frac{\pi \ell(t)}{2}}. \quad (28)$$

Equations (27) and (28) are the most general energy release and stress intensity factors that can be retrieved using scaling arguments. Because LEFM does not involve intrinsic length or time scales, the function  $g(v)$  depends only on the instantaneous speed  $v(t)$  and on the loading mode (tensile, shear or anti-plane) as long as the following conditions are ensured: small-scale yielding, the crack is the only source of wave radiation and there are no discontinuous changes in either loading conditions or the dissipation processes. Notice that  $g(v)$  has been analytically computed so far for two particular cases: the semi-infinite propagating crack and the self-similar crack growth<sup>22,23</sup>. Nevertheless, a Mott-like argument<sup>22</sup> shows that  $g(v)$  is always a decreasing function of  $v(t)$  satisfying  $g(0) = 1$ , so that the energy release rate coincides with its quasi-static value. As shown in the main text, these two properties are sufficient to establish general results for the nucleation of failure.

To make the general arguments presented here more concrete, let us now consider a specific example, the case of a perfect penny shape self-similar crack growth of radius  $R(t)$  (Extended Data Fig. 6). At the beginning of the rupture process, the crack surface is bounded by a circular contour. If the growth is sustained, the penny crack front reaches the free boundaries and transitions to a regime in which two disconnected fronts propagate in opposite directions. We assume that this regime also preserves the self-similarity such that the broken area consists of a surface bounded by either a circle of radius  $R(t)$  (when  $R < W/2$ ) or (in the through-crack regime) the lines  $z = \pm W/2$ . For a

circular ‘penny’ crack, the perimeter  $P(t)$  and area  $A(t)$  of such a propagating crack are then given by

$$P(R) = \begin{cases} 2\pi R & R < \frac{W}{2} \\ 4R \arcsin \frac{W}{2R} & R > \frac{W}{2} \end{cases} \quad (29)$$

$$A(R) = \begin{cases} \pi R^2 & R < \frac{W}{2} \\ 2R^2 \left[ \arcsin \frac{W}{2R} + \frac{W}{2R} \sqrt{1 - \left( \frac{W}{2R} \right)^2} \right] & R > \frac{W}{2} \end{cases} \quad (30)$$

Using equation (24), we find that the crack length of the 2D mapped configuration satisfies  $\ell(t) = 2R(t)$  and  $\ell^* = W$ . Consequently, the shape factor  $\beta(t)$  defined by equation (26) is given by

$$\beta(\ell) = \begin{cases} \frac{\pi}{2} & \ell < W \\ \arcsin \frac{W}{\ell} & \ell > W \end{cases}. \quad (31)$$

The result  $\beta(\ell) = \pi/2$  for  $\ell < W$  corresponds to the lower bound of the shape factor. However, the result that  $\beta(\ell)$  is constant still holds for any self-similar propagation in the penny-like regime, not only when the crack shape is a circle.

The self-similar behaviour allows us to use Broberg’s results for the function  $g(v)$  involved in equation (27). The function  $g(v)$  is shown in Extended Data Fig. 6 for both mode I ( $g(v) \equiv g_1(v)$ ) and mode II ( $g(v) \equiv g_2(v)$ ) loading and its analytical form can be found in ref. 23. It is straightforward to show that we can solve the equation of motion of the crack in both phases and the results are shown in Extended Data Fig. 7. For the penny-like regime  $\ell(t) < W$ , the nucleated defect will propagate at a constant speed if and only if  $\sigma > \Sigma_c = \sqrt{E\Gamma/W}$ . As expected, the crack will accelerate after the topological transition to the through-crack-like regime  $\ell > W$ . Finally, as  $v$  is constant for  $\ell(t) \leq W$ , we can easily compute a critical nucleation time  $T$  before complete failure. Therefore, the behaviour in the penny-like regime can be described as a geometric creep characterized by a constant speed of a growing defect that is controlled by the departure from the critical stress  $\Sigma_c$ .

## Data availability

The raw data (camera recordings and strain gauge measurements) for all events analysed in this paper can be accessed directly at <https://doi.org/10.4121/12631fa1-4fed-440d-acf3-676b97862034>. More information and other findings of this study are available from the corresponding author upon request. Source data are provided with this paper.

**Acknowledgements** J.F. and S.G. acknowledge the support of the Israel Science Foundation (grant no. 416/23).

**Author contributions** S.G. performed the experimental measurements. S.G. and J.F. contributed to the data analysis and experimental design. M.A-B. led the derivation of the theory, with contributions from the other authors. D.S.K. performed all of the numerical work. All authors contributed to the writing of the paper and overall analysis.

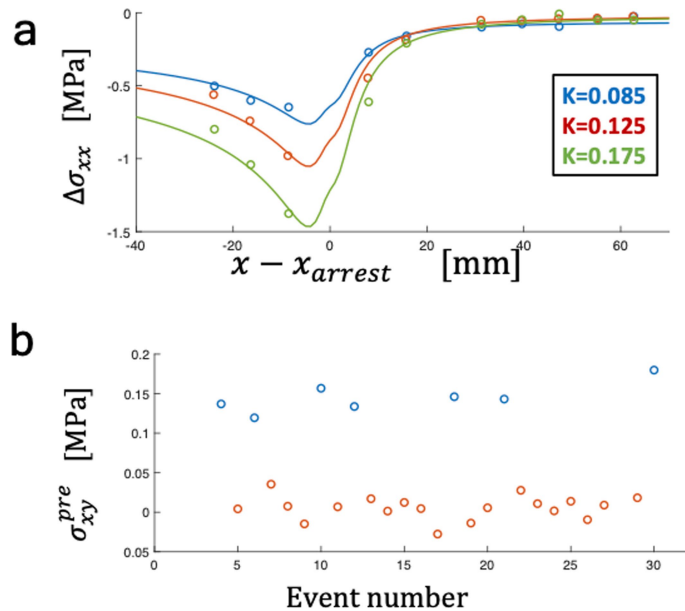
**Competing interests** The authors declare no competing interests.

### Additional information

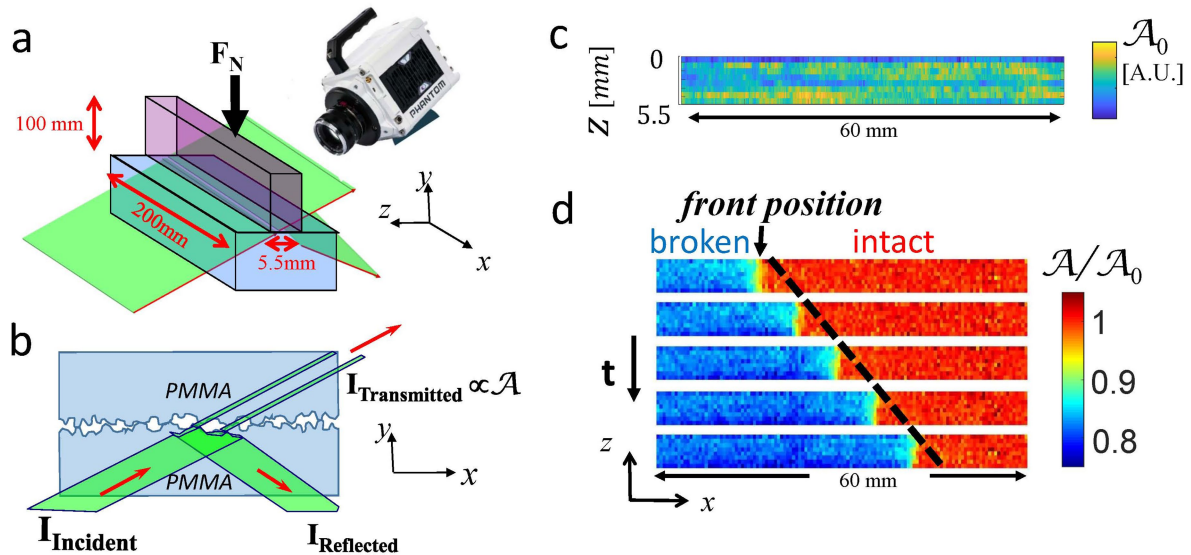
**Correspondence and requests for materials** should be addressed to Jay Fineberg.

**Peer review information** *Nature* thanks the anonymous reviewers for their contribution to the peer review of this work.

**Reprints and permissions information** is available at <http://www.nature.com/reprints>.



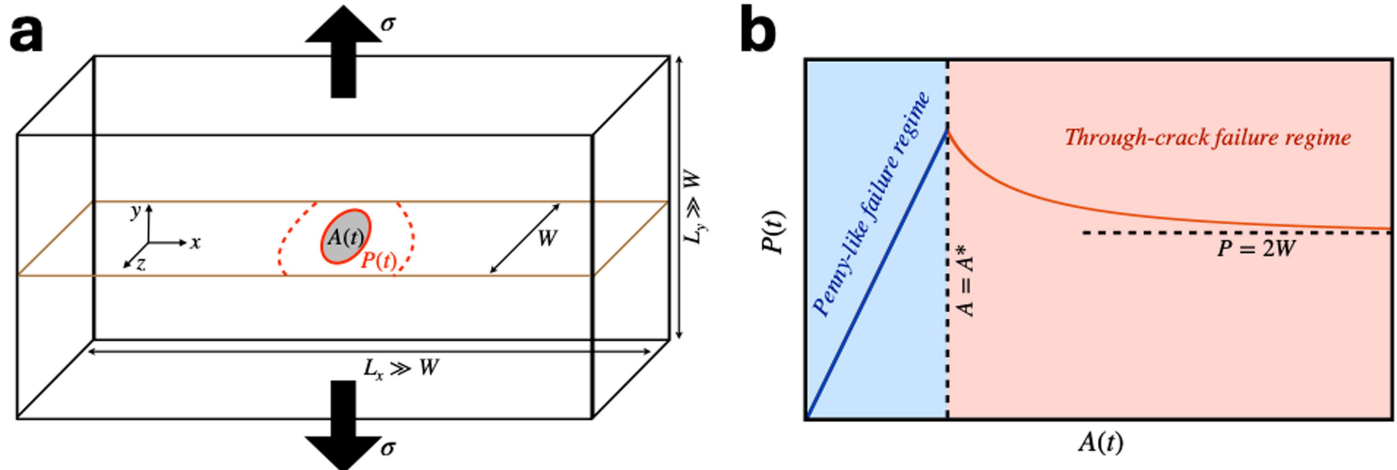
**Extended Data Fig. 1 | The stress intensity factor  $K$  of an arrested rupture is determined by strain gage measurements.** **a.** Strain gage measurements (symbols) of the measured stress changes,  $\Delta\sigma_{xx}$ , excited by a rupture that arrested at point  $x_{arrest}$ , as a function of  $x - x_{arrest}$ . Fitted LEFM predictions (see Eq. (6)) (lines) compare well with the strain gage measurements, when  $K$  is the sole fitting parameter. Shown are 3 different events, each with a different value of  $v_{arr}$ , the rupture velocity immediately prior to rupture arrest at imposed barriers. **b.** The initial ‘pre-stress’ data,  $\sigma_{xy}^{pre}$ , measured at the nucleation site in a single sequence of 30 induced nucleation events. Red symbols are events in which the previous arrested rupture triggered a nucleation event. In these cases  $\sigma_{xy}^{pre} \neq 0$ . Blue symbols denote  $\sigma_{xy}^{pre}$  for events in which the previous arrested rupture did *not* trigger a nucleation event. These finite pre-stresses need to be accounted for to correctly determine the shear stress,  $\tau$ , at the nucleation site.



**Extended Data Fig. 2 | The real contact area and rupture front positions are determined optically.** (a,b) Imaging system - the entire contact interface was illuminated by a sheet of incoherent light directed at an incident angle 28° beyond the critical angle (41.8°) for total internal reflection from PMMA to air. Light impinging on non-contacting regions of the interface was reflected away from the interface. Incident light was only transmitted through the interface at the points of contact. The transmitted light was recorded at 580000 frames/sec by a fast camera (Phantom V711) at an  $x \times z$  spatial resolution of

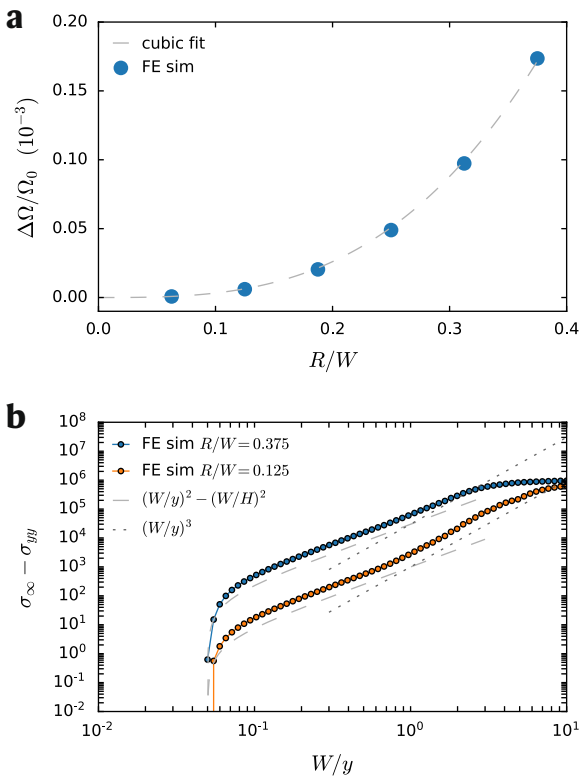
1280  $\times$  8 pixels. **c**. Close up of a non-normalized image. The light intensity<sup>10</sup> at each point yields a rough topographic image of the contacting points (each  $x, z$  pixel is mapped to an area of 156  $\times$  688  $\mu$ m that contains about 1000 contacts). **d**. Temporal sequence of normalized contact areas,  $\mathcal{A}(x, z, t)/\mathcal{A}_0(x, z)$ , in which the motion of the (effectively 1D) rupture front propagating at approximately 1000m/s (0.8 $C_R$ ) is evident. The  $x, z$  dimensions are as in **c**. Intervals between frames are 3.4  $\mu$ s.

# Article



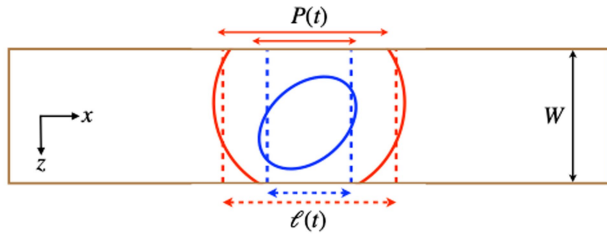
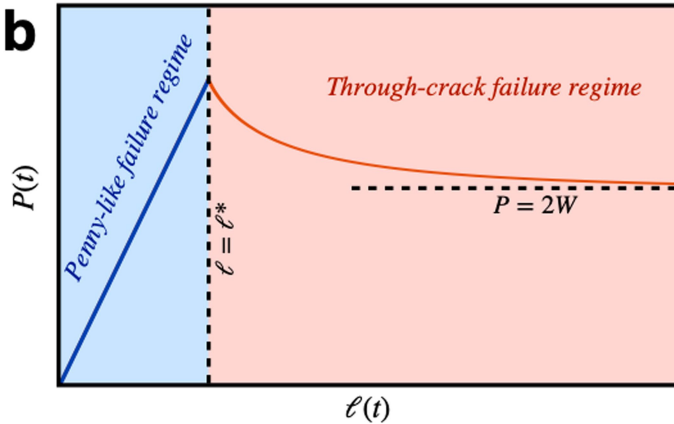
**Extended Data Fig. 3 | In a spatially confined interface, the rupture area and perimeter are independent entities, until the topological transition to a 1D rupture front.** **a.** Schematic representation of the generic problem of

failure nucleation in a confined geometry. **b.** Schematic evolution of the rupture: the perimeter  $P(t)$  of the crack front as function of its area  $A(t)$ .

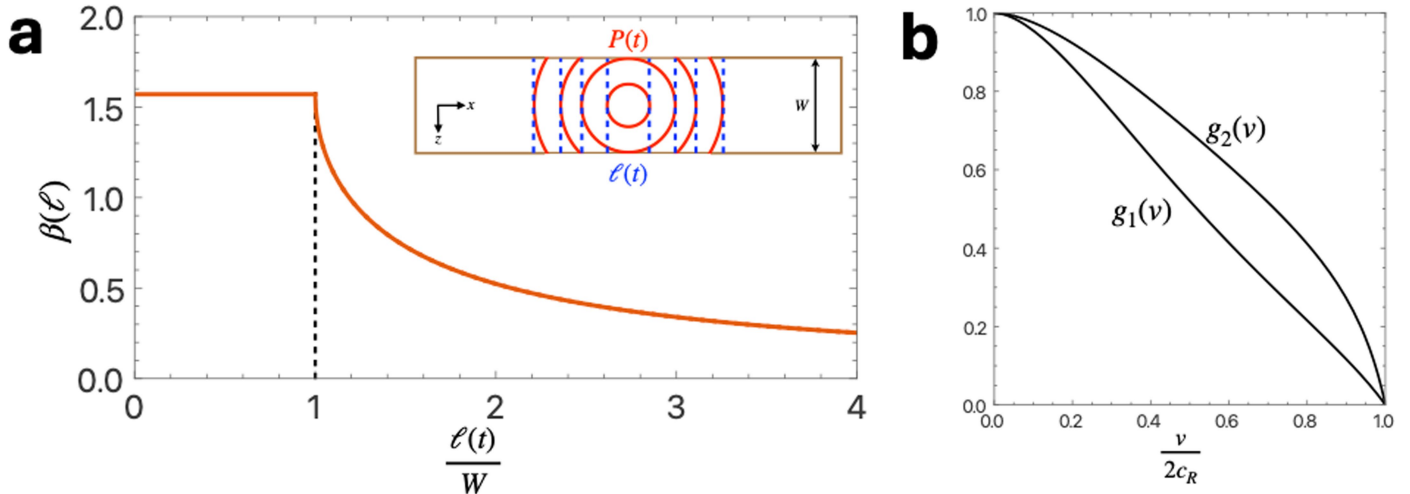


**Extended Data Fig. 4 | The stress released by a nucleation patch changes its character from ‘penny crack’ scaling to ‘through crack’ scaling with the distance from the patch.** Numerical results from FE simulations. **a.** Normalized excess potential energy as a function of crack radius  $R$ . The dashed line is the least squares cubic fit:  $\Delta\Omega/\Omega_0 = 3.25(R/W)^3$ . **b.** Tensile stress  $\sigma_{yy}$  difference along a line perpendicular to the crack plane starting from its center, for two different  $R/W$  ratios. Trends, corresponding to the scaling derived in Eq. (15), are shown in dashed (far field) and dotted (near field) gray lines.

# Article

**a****b**

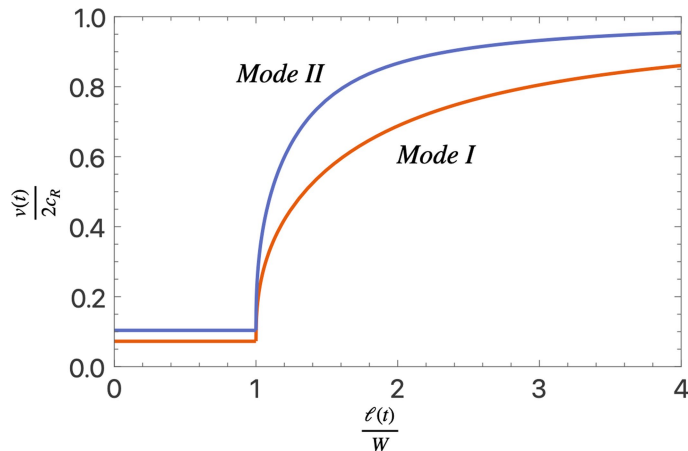
**Extended Data Fig. 5 | As the mapped ‘1D’ crack length approaches  $W$ , a topological transition from the ‘penny-like’ to ‘through-crack’ failure regimes occurs.** **a.** Schematic view of 3D rupture propagation in a confined geometry. The rupture is characterized by its perimeter  $P(t)$  and the enclosed area,  $A(t)$ . These are mapped to the 2D configuration characterized by a straight crack front of length  $\ell(t)$ . **b.** The generic behavior of the perimeter  $P(t)$  in the original problem as function of the crack length  $\ell(t)$  in the mapped configuration.



**Extended Data Fig. 6 | The shape function,  $\beta(\ell)$ , characterizing self-similar nucleation patches is particularly simple during the nucleation phase, until the topological transition to 1D rupture occurs at  $\ell'$ . a.** The shape function  $\beta(\ell)$  for a self-similar growth of a penny crack shown in the inset. Note that, in this case,  $\beta = \pi/2$  for  $\ell < \ell' = W$ , where  $\ell'$  is the value of  $\ell$  at which the

topological transition takes place. **b.** Mode I ( $g_1(v)$ ) and mode II ( $g_2(v)$ ) solutions of self-similar Broberg problems<sup>23</sup>. Here, plane stress conditions are imposed so that the dilatational ( $c_d$ ) and shear ( $c_s$ ) wave speeds are related by  $c_d = \sqrt{2/(1-\rho)} c_s$ , where  $\rho=1/3$  is the Poisson ratio.

## Article



**Extended Data Fig. 7 | The transition from slow nucleation to rapid ‘1D’ dynamics for a self-similar nucleation patch.** The dynamics of tensile (mode I) and shear (mode II) rupture fronts corresponding to the case depicted in Extended Data Fig. 6 with  $L_c \approx 0.62W$ .